

## CHIME-o-Grav: Wideband Timing of Four Millisecond Pulsars from the NANOGrav 15-yr dataset

GABRIELLA Y. AGAZIE <sup>1</sup>, DAVID L. KAPLAN <sup>1</sup>, ABHIMANYU SUSOBHANAN <sup>2</sup>, INGRID H. STAIRS <sup>3</sup>,  
DEBORAH C. GOOD <sup>4</sup>, BRADLEY W. MEYERS <sup>5,6</sup>, EMMANUEL FONSECA <sup>7,8</sup>, TIMOTHY T. PENNUCCI <sup>9</sup>,  
AKASH ANUMARLAPUDI <sup>10</sup>, ANNE M. ARCHIBALD <sup>11</sup>, ZAVEN ARZOUMANIAN <sup>12</sup>, PAUL T. BAKER <sup>13</sup>,  
PAUL R. BROOK <sup>14</sup>, ALYSSA CASSITY <sup>3</sup>, H. THANKFUL CROMARTIE <sup>15</sup>, KATHRYN CROWTER <sup>3</sup>,  
MEGAN E. DECESAR <sup>16,\*</sup>, PAUL B. DEMOREST <sup>17</sup>, TIMOTHY DOLCH <sup>18,19</sup>, FENGQIU ADAM DONG <sup>20</sup>,  
ELIZABETH C. FERRARA <sup>21,22,23</sup>, WILLIAM FIORE <sup>3</sup>, GABRIEL E. FREEDMAN <sup>23</sup>, NATE GARVER-DANIELS <sup>7,8</sup>,  
PETER A. GENTILE <sup>7,8</sup>, JOSEPH GLASER <sup>7,8</sup>, JEFFREY S. HAZBOUN <sup>24</sup>, ROSS J. JENNINGS <sup>7,8,†</sup>,  
MEGAN L. JONES <sup>1</sup>, MATTHEW KERR <sup>25</sup>, MICHAEL T. LAM <sup>26,27,28</sup>, DUNCAN R. LORIMER <sup>7,8</sup>, JING LUO <sup>29,‡</sup>,  
RYAN S. LYNCH <sup>30</sup>, ALEXANDER MCEWEN <sup>1</sup>, JAMES W. MCKEE <sup>31</sup>, MAURA A. MCLAUGHLIN <sup>7,8</sup>,  
NATASHA MCMANN <sup>32</sup>, CHERRY NG <sup>33</sup>, DAVID J. NICE <sup>34</sup>, BENETGE B. P. PERERA <sup>35</sup>, NIHAN S. POL <sup>36</sup>,  
HENRI A. RADOVAN <sup>37</sup>, SCOTT M. RANSOM <sup>20</sup>, PAUL S. RAY <sup>25</sup>, ALEXANDER SAFFER <sup>20,†</sup>, ANN SCHMIEDEKAMP <sup>38</sup>,  
CARL SCHMIEDEKAMP <sup>38</sup>, BRENT J. SHAPIRO-ALBERT <sup>7,8,39</sup>, KEVIN STOVALL <sup>17</sup>, JOSEPH K. SWIGGUM <sup>34,†</sup>,  
MERCEDES S. THOMPSON <sup>3</sup> AND HALEY M. WAHL <sup>7,8</sup>

<sup>1</sup>Center for Gravitation, Cosmology and Astrophysics, Department of Physics and Astronomy, University of Wisconsin-Milwaukee, P.O. Box 413, Milwaukee, WI 53201, USA

<sup>2</sup>Max-Planck-Institut für Gravitationsphysik (Albert-Einstein-Institut), Callinstraße 38, D-30167 Hannover, Germany  
Leibniz Universität Hannover, D-30167 Hannover, Germany

<sup>3</sup>Department of Physics and Astronomy, University of British Columbia, 6224 Agricultural Road, Vancouver, BC V6T 1Z1, Canada

<sup>4</sup>Department of Physics and Astronomy, University of Montana, 32 Campus Drive, Missoula, MT 59812

<sup>5</sup>Australian SKA Regional Centre (AusSRC), Curtin University, Bentley, WA 6102, Australia

<sup>6</sup>International Centre for Radio Astronomy Research (ICRAR), Curtin University, Bentley, WA 6102, Australia

<sup>7</sup>Department of Physics and Astronomy, West Virginia University, P.O. Box 6315, Morgantown, WV 26506, USA

<sup>8</sup>Center for Gravitational Waves and Cosmology, West Virginia University, Chestnut Ridge Research Building, Morgantown, WV 26505, USA

<sup>9</sup>Institute of Physics and Astronomy, Eötvös Loránd University, Pázmány P. s. 1/A, 1117 Budapest, Hungary

<sup>10</sup>Department of Physics and Astronomy, University of North Carolina, Chapel Hill, NC 27599, USA

<sup>11</sup>Newcastle University, NE1 7RU, UK

<sup>12</sup>X-Ray Astrophysics Laboratory, NASA Goddard Space Flight Center, Code 662, Greenbelt, MD 20771, USA

<sup>13</sup>Department of Physics and Astronomy, Widener University, One University Place, Chester, PA 19013, USA

<sup>14</sup>Institute for Gravitational Wave Astronomy and School of Physics and Astronomy, University of Birmingham, Edgbaston, Birmingham B15 2TT, UK

<sup>15</sup>National Research Council Research Associate, National Academy of Sciences, Washington, DC 20001, USA resident at Naval Research Laboratory, Washington, DC 20375, USA

<sup>16</sup>Department of Physics and Astronomy, George Mason University, Fairfax, VA 22030, resident at the U.S. Naval Research Laboratory, Washington, DC 20375, USA

<sup>17</sup>National Radio Astronomy Observatory, 1003 Lopezville Rd., Socorro, NM 87801, USA

<sup>18</sup>Department of Physics, Hillsdale College, 33 E. College Street, Hillsdale, MI 49242, USA

<sup>19</sup>Eureka Scientific, 2452 Delmer Street, Suite 100, Oakland, CA 94602-3017, USA

<sup>20</sup>National Radio Astronomy Observatory, 520 Edgemont Road, Charlottesville, VA 22903, USA

<sup>21</sup>Department of Astronomy, University of Maryland, College Park, MD 20742, USA

<sup>22</sup>Center for Research and Exploration in Space Science and Technology, NASA/GSFC, Greenbelt, MD 20771

<sup>23</sup>NASA Goddard Space Flight Center, Greenbelt, MD 20771, USA

<sup>24</sup>Department of Physics, Oregon State University, Corvallis, OR 97331, USA

<sup>25</sup>Space Science Division, Naval Research Laboratory, Washington, DC 20375-5352, USA

<sup>26</sup>SETI Institute, 339 N Bernardo Ave Suite 200, Mountain View, CA 94043, USA

<sup>27</sup>School of Physics and Astronomy, Rochester Institute of Technology, Rochester, NY 14623, USA

<sup>28</sup>Laboratory for Multiwavelength Astrophysics, Rochester Institute of Technology, Rochester, NY 14623, USA

<sup>29</sup>Department of Astronomy & Astrophysics, University of Toronto, 50 Saint George Street, Toronto, ON M5S 3H4, Canada

<sup>30</sup>*Green Bank Observatory, P.O. Box 2, Green Bank, WV 24944, USA*

<sup>31</sup>*Department of Physics and Astronomy, Union College, Schenectady, NY 12308, USA*

<sup>32</sup>*Department of Physics and Astronomy, Vanderbilt University, 2301 Vanderbilt Place, Nashville, TN 37235, USA*

<sup>33</sup>*Dunlap Institute for Astronomy and Astrophysics, University of Toronto, 50 St. George St., Toronto, ON M5S 3H4, Canada*

<sup>34</sup>*Department of Physics, Lafayette College, Easton, PA 18042, USA*

<sup>35</sup>*Arecibo Observatory, HC3 Box 53995, Arecibo, PR 00612, USA*

<sup>36</sup>*Department of Physics, Texas Tech University, Box 41051, Lubbock, TX 79409, USA*

<sup>37</sup>*Department of Physics, University of Puerto Rico, Mayagüez, PR 00681, USA*

<sup>38</sup>*Department of Physics, Penn State Abington, Abington, PA 19001, USA*

<sup>39</sup>*Giant Army, 915A 17th Ave, Seattle WA 98122*

## Abstract

Wideband timing of the the North American Nanohertz Observatory for Gravitational Waves (NANOGrav) datasets was first done for the 12.5 yr dataset. This method, where a single time-of-arrival (TOA) and a single dispersion measure (DM) are measured using the entire bandwidth of each observation, proved to be invaluable for characterizing the time-varying dispersion measure, improving handling of frequency dependent profile variability, and data volume reduction. The Canadian Hydrogen Intensity Mapping Experiment (CHIME) Telescope has been observing most NANOGrav millisecond pulsars (MSPs) at nearly daily cadence (compared to roughly monthly cadence for other NANOGrav observations) since 2019 with the objective of integration into future pulsar timing array (PTA) datasets. In this paper, we show the results of integration of high-cadence, low-observing-frequency CHIME data with data from the NANOGrav experiment for an isolated MSP PSR J0645+5158 and three binary MSPs PSR J1012+5307, PSR J2145–0750, and PSR J2302+4442. Using a wideband timing pipeline which we also describe, we present updated timing results for all four sources, including improved relativistic post-Keplerian measurements for the three binary pulsars in this analysis. For PSR J2302+4442, we report an updated strong detection of Shapiro delay from which we measured a companion mass of  $0.35^{+0.05}_{-0.04} M_{\odot}$ , a pulsar mass of  $1.8^{+0.3}_{-0.3} M_{\odot}$ , and an orbital inclination of  $80^{\circ}_{-2}^{+1}$ . We also report updated constraints on the reflex motion for PSR J2145–0750 using a combination of Very Long Baseline Array astrometry and our updated measurement of the time derivative of the projected semi-major axis of the pulsar orbit as a prior.

## 1. INTRODUCTION

Pulsars are a class of highly magnetized neutron stars characterized by beams of electromagnetic radiation emanating from each magnetic pole which terrestrial observers detect as a pulsed emission (Lorimer 2008). They have densities comparable to atomic nuclei and are useful laboratories for studying extreme states of matter, placing constraints on the nuclear equation of state, and testing theories of gravity (Burgio et al. 2021; Lorimer & Kramer 2012).

Millisecond pulsars (MSPs) are a class of pulsars that have very low spin periods ( $P \lesssim 30$  ms) and low period derivatives ( $\dot{P} \lesssim 10^{-19}$  s s<sup>-1</sup>). Many MSPs form in binaries where the kick from the explosion of the supernovae of the pulsar progenitor does not disrupt the binary (Bhattacharya & van den Heuvel 1991). Over time matter from the companion is accreted by the pulsar by

Roche Lobe overflow and the corresponding transfer of angular momentum speeds up the pulsar’s rotation to millisecond spin periods (Alpar et al. 1982). These systems typically become white dwarf-MSP binaries with nearly circular orbits (Phinney 1992). Pulsar timing arrays (PTAs) are constructed from long term timing campaigns of MSPs and are used to search for nanohertz frequency gravitational waves which manifest as correlated perturbations in pulse times-of-arrival (TOA) residuals from different pulsars (Hellings & Downs 1983; Agazie et al. 2023a; EPTA Collaboration et al. 2023; Miles et al. 2025; Reardon et al. 2023; Xu et al. 2023).

High-precision timing of binary MSPs can also be used to probe parameters of the nuclear equation of state such as neutron star masses, radii, and system inclinations (Özel & Freire 2016). In pulsar binaries, we can measure relativistic corrections to the Keplerian orbital model which are represented in pulsar ephemerides as post-Keplerian (PK) parameters. Measurement of a single PK parameter, such as the relativistic orbital decay ( $\dot{P}_B$ ), can place constraints on possible combinations of pulsar and companion masses by defining a curve in

\* Resident at the Naval Research Laboratory

† NANOGrav Physics Frontiers Center Postdoctoral Fellow

‡ Deceased

companion-pulsar mass space (Taylor & Weisberg 1982). Shapiro delay, which is caused by pulsar signal passing through the curved spacetime around companion star, is typically measured in nearly edge-on orbits and is parameterized by two PK parameters, range ( $r$ ) and shape ( $s$ ) (Shapiro 1964; Damour & Deruelle 1986). These parameters can be used to get measurements of the pulsar and companion masses as well as the system inclination (Freire & Wex 2010). Having three or more measured PK parameters makes the system over-determined, allowing it to be used to test theories of gravity (Burgio et al. 2021).

### 1.1. Wideband Timing

TOAs are usually calculated by cross-correlating observed pulse profiles with a noise-free template of the integrated pulse profile (Lorimer & Kramer 2012). In traditional narrowband timing this template is frequency-averaged and does not account for evolution of the pulse profile across the observing bandwidth. When timing pulsars, we can expect some evolution of the pulse profile shape as a function of frequency caused by intrinsic changes in the pulsar magnetosphere, and extrinsic effects such as interstellar scattering and frequency-dependent dispersion measure (DM) (Hankins & Rickett 1986; Alam et al. 2021a). Narrowband timing methods typically deal with profile evolution by calculating TOAs at several different frequencies in a single observation and the inclusion of arbitrary frequency dependent parameters in the timing model (Alam et al. 2021b).

Wideband (WB) timing is a method of using a smooth 2-D frequency-dependent model of the pulse profile, often called a template portrait, to simultaneously measure a TOA and a dispersion measure (DM) from each observation, without splitting the observations into multiple frequency sub-bands (Pennucci et al. 2014). The reference frequency for the TOA is selected such that there is zero covariance between the TOA phase offset and DM measurement. WB template portraits are calculated from high signal to noise (S/N) data portraits, which are constructed by aligning and averaging many observations with strong detections of the pulsar together (Pennucci 2019).

To construct the template portrait, the mean (frequency-averaged) profile-subtracted data portrait is decomposed into an orthonormal set of eigenprofiles using principal component analysis (PCA). A small number of the eigenprofiles are kept as the basis for constructing the profile evolution model. The eigenprofiles and the mean profile are then de-noised using a Stationary Wavelet Transform (Lee et al. 2019). Coordinate functions of the profile evolution are constructed

by projecting the de-noised eigenprofiles onto the de-noised mean profile. These are then approximated by fitting a spline to each coordinate function. The coordinate function splines and de-noised mean profile are used to construct the 2-D template portrait which is then used for calculation WB TOAs.

Calculating TOAs with this method means that individual wideband TOAs often have much greater precision than individual narrowband TOAs derived from the same data. Only one wideband TOA measurement need be made from a single observation to cover the total observing bandwidth, whereas multiple narrowband TOAs are needed to cover the total bandwidth and then are fit simultaneously, with a final precision comparable to that of the wideband data. However, using multiple narrowband TOAs may require arbitrary frequency dependent parameters in the timing model because profile evolution is handled at the timing stage rather than the profile template creation stage. The use of wideband timing significantly reduces the TOA volume in large PTA datasets, lowers the number of free parameters in the timing model, and more smoothly handles frequency dependent profile variability when compared to narrowband timing (Johnson et al. 2024; Agazie et al. 2023b; Alam et al. 2021a).

### 1.2. The Canadian Hydrogen Intensity Mapping Experiment

The Canadian Hydrogen Intensity Mapping Experiment (CHIME) Telescope is a drift scan radio telescope that has been observing sources in the NANOGrav pulsar timing array with nearly daily cadence since 2019 (The CHIME Collaboration et al. 2022; Good 2021). In this paper, we present results of wideband data combination of CHIME data with that from the NANOGrav 15 year dataset (NG15) for four pulsars: PSR J0645+5158, PSR J1012+5307, PSR J2145–0750, and PSR J2302+4442. In Section 2 we describe the instruments used for observing and the data reduction techniques used to calculate the CHIME WB TOAs. Section 3 describes the binary models, DM modeling, and noise modeling used for the timing analysis of the combined CHIME/NG15 dataset. Section 4 reports timing analysis results for each source, and Section 5 discusses the impact of the inclusion of CHIME data of our timing results. Finally, Section 6 summarizes our major conclusions and areas for future work.

## 2. OBSERVATIONS AND DATA REDUCTION

The observations for all four sources in this analysis were conducted on both the Robert C. Byrd Green Bank Telescope (GBT) and CHIME telescopes. All GBT data

used in this analysis came from the NANOGrav observing program as described in [Agazie et al. \(2023b\)](#). The total observing time span for GBT data varies for each source based on when each was included in the observing program and is listed in Table 1.

### 2.1. GBT

For each observing epoch, the GBT data were taken with both the 820-MHz and L-Band (1.4 GHz) receivers with roughly monthly cadence. The dual-frequency observations are used to improve timing precision and dispersion measure (DM) estimates. Data collected prior to 2011 for PSR J1012+5307 and PSR J2145–0750 used the GASP pulsar backend (64 MHz bandwidth with 4 MHz frequency resolution) ([Demorest 2007](#); [Agazie et al. 2023b](#)). All other data were collected using the Green Bank Ultimate Pulsar Processing Instrument (GUPPI) backend using 2048 frequency bins. For this backend the 820-MHz receiver has a 160 MHz bandwidth with a time resolution of  $81.92 \mu\text{s}$  and 2048 frequency bins. The L-Band receiver has a 640 MHz bandwidth centered at 1500 MHz with a time resolution of  $40.96 \mu\text{s}$  and 2048 frequency bins. Times of arrival (TOAs) used in the timing analysis were published in the NANOGrav 15-yr data release [Agazie et al. \(2023b\)](#).

### 2.2. CHIME

Data from the CHIME telescope used in this analysis were collected between April 2019 and March 2023 at nearly daily cadence. The CHIME/Pulsar backend collects 10 beamformed voltages with a frequency range of 400–800 MHz, time resolution of  $2.56 \mu\text{s}$ , and frequency resolution of 0.390625 MHz ([The CHIME Collaboration et al. 2022](#); [CHIME/Pulsar Collaboration et al. 2021](#)). Observation lengths were determined by a transit duration, typically 10–15 minutes for all sources.

### 2.3. Data Reduction

Data processing prior to the step of calculation of TOAs was done using the `psrchive`<sup>40</sup> software suite with different procedure pipelines used for NG15 data vs CHIME data. For NG15 data this was done using the `nanopipe`<sup>41</sup> data reduction pipeline which included radio frequency interference (RFI) excision, flux and polarization calibration, frequency scrunching to 64 channels, and time scrunching to a single sub-integration.

For CHIME data, we developed a data processing pipeline `chimera` ([Susobhanan 2026](#)) to perform equivalent processing steps to those in `nanopipe` specifically

for generating WB TOAs. This pipeline is described in Appendix A. The exception being that we did not do polarization calibration of the CHIME data, as calibration methods for CHIME are still under development ([CHIME/Pulsar Collaboration et al. 2021](#)). Polarization calibration would account for instrumental polarization distortions which could introduce systemic errors into TOA calculations if not corrected for ([van Straten 2026](#)). These errors can be particularly pronounced for sources with a high polarization fraction as the pulsar signal passing through the interstellar medium can also undergo significant Faraday rotation. Of the sources in this analysis, PSR J1012+5307 and PSR J2145–0750 have been previously observed to have significant polarization fractions of 0.66 and 0.21 respectively ([Wahl et al. 2022](#)). Introducing polarization calibration in future analyses could account for instrumental errors, reduce TOA uncertainty, and improve timing rms residuals.

### 2.4. WB Template Portraits

Generation of WB template portraits and TOA calculation was done using the `PulsePortraiture`<sup>42</sup> software suite ([Pennucci 2019](#)). WB template portraits are made by first constructing a high S/N data portrait by adding and aligning all observations from a given receiver together using `ppalign.py`. From these data portraits, the template portraits are calculated using a combination of principal component analysis and spline interpolation using `ppspline.py`. The choice of the number of significant eigenprofiles was done using an S/N threshold of 150, which was calculated using methods from [Pennucci \(2019\)](#) and [NANOGrav Collaboration et al. \(2015\)](#).

WB template portraits do not inherently account for instrument offsets and are not accurate beyond the observing frequency range of the data portrait ([Pennucci 2019](#)). The WB template portraits used for NG15 data were the same as those used in [Alam et al. \(2021a\)](#). We required the calculation of new CHIME-specific template portraits for each source. To avoid the inclusion of noisy or marginal detections, only observations with an S/N exceeding an empirically determined threshold, we chose the 50th percentile of S/N per pulsar, were included in the construction of the data portraits. This threshold was 60 for PSR J1012+5307 and 20 for PSR J0645+5158, J2145–0750, and J2302+4442.

<sup>40</sup> <https://psrchive.sourceforge.net/>

<sup>41</sup> <https://github.com/demorest/nanopipe>

<sup>42</sup> <https://github.com/pennucci/PulsePortraiture>

**Table 1.** TOA Statistics and fit results.  $N_{\text{toas}}$  is the number of TOAs per dataset per pulsar.

Source	J0645+5158	J1012+5307	J2145–0750	J2302+4442
CHIME $N_{\text{toas}}$	1099	1070	1036	1046
NG15 $N_{\text{toas}}$	281	630	400	237
MJD span	55704 – 60000	53267 – 60000	53267 – 60000	55972 – 60000
NG15 MJD span	55704 – 58939	53267 – 58939	53267 – 58942	55972 – 58942
CHIME MJD span	58602 – 60000	58700 – 60000	58646 – 60000	58646 – 60000
TOA rms ( $\mu\text{s}$ )	0.3097	0.6037	0.8337	1.9596
DM rms ( $\text{pc cm}^{-3}$ )	0.000155	0.000222	0.00109	0.000824
$\chi_{\text{red}}^2$	1.858	1.924	2.300	1.098

**Table 2.** Timing Results for spin, binary, astrometric, and PK parameters. Reported DMs represent the central DM for the DMX model. DMX parameters are not listed for brevity. Derived parameters are indicated with an asterisk.  $N_{\text{DMX}}$  represents the number of DMX parameters used per pulsar for the preferred DMX model (Table 3). Actual DMX values are omitted for brevity.

Source	J0645+5158	J1012+5307	J2145–0750	J2302+4442
Right Ascension (J2000)	6:45:59.082669(3)	10:12:33.438837(3)	21:45:50.457730(2)	23:02:46.9787911(3)
Declination (J2000)	51:58:14.88593(5)	53:07:02.18562(2)	–7:50:18.52879(13)	44:42:22.06555(13)
$P$ (s)	0.008853496686733226(8)	0.005255749022591625(8)	0.016052423674578594(3)	0.005192324649748711(12)
$\dot{P}$ ( $10^{-20} \text{ s s}^{-1}$ )	0.4922052(9)	1.71274(2)	2.979272(5)	1.38704(3)
DM ( $\text{pc cm}^{-3}$ )	18.2476	9.0224	9.00369	13.7234
$N_{\text{DMX}}$	404	471	438	99
$\mu_{\alpha}$ ( $\text{mas yr}^{-1}$ )	1.516(11)	2.620(6)	–9.71(11)	0.0849(5)
$\mu_{\delta}$ ( $\text{mas yr}^{-1}$ )	–7.465(17)	–25.529(4)	–8.77(4)	–5.60(4)
$\varpi$ (mas)	0.75(9)	1.0(10)	1.58(5)	0.6(6)
Binary Parameters				
Binary Model	...	ELL1	ELL1H	ELL1H
$P_{\text{b}}$ (days)	...	0.6046727138556(27)	6.838902509666(19)	125.935296927(6)
$e$ *	...	$1.46(8) \times 10^{-6}$	$1.9320(6) \times 10^{-5}$	0.000503015(9)
$\omega$ (deg) *	...	83.1(3.3)	200.93(15)	207.8855(12)
$T_0$ (MJD) *	...	56428.286(5)	56591.8268(4)	57813.8837(4)
$x$ (ls)	...	0.581817940(31)	10.16410970(4)	51.4299730(13)
$\epsilon_1$	...	$1.5(1) \times 10^{-6}$	$-6.902(3) \times 10^{-6}$	$-2.35248(4) \times 10^{-4}$
$\epsilon_2$	...	$8(111) \times 10^{-9}$	$-1.8042(4) \times 10^{-5}$	$-4.44579(4) \times 10^{-4}$
$T_{\text{ASC}}$ (MJD)	...	56339.86402951(12)	56588.009633654(3)	57993.02901376(5)
Post-Keplerian Parameters				
$\dot{P}_{\text{b}}$ ( $10^{-14}$ )	...	5.3(12)	...	...
$\dot{x}$ ( $10^{-15} \text{ ls s}^{-1}$ )	...	1.62(19)	10.2(2)	...
$m_{\text{c}}$ ( $M_{\odot}$ ) *	...	...	...	0.32(9)
$\sin i$ *	...	...	...	0.990(11)
$h_3$ (s)	...	...	$6(1.3) \times 10^{-8}$	$1.04(5) \times 10^{-6}$
$\varsigma$	...	...	...	0.84(2)
NHARMS	...	...	3	...

### 3. TIMING ANALYSIS

Timing was done using the PINT<sup>43</sup> software package (Luo et al. 2021; Susobhanan et al. 2024). To build the timing models for the combined CHIME/NG15 TOAs for each pulsar, we started with the NANOGrav 15-yr ephemeris and included new JUMP and DMJUMP parameters for the CHIME receiver. These account for any constant phase or DM offsets between receivers. Timing ephemeris are reported in Table 2 with fit results and TOA statistics reported in Table 1.

#### 3.1. Binary Modeling

All three binary pulsars in this analysis PSR J1012+5307, PSR J2145–0750, and PSR J2302+4442, have nearly circular orbits. Periastron is poorly defined in orbits with low eccentricity, thus requiring the use of Lagrange Laplace terms  $\epsilon_1$  and  $\epsilon_2$  over the typical Keplerian parameters, eccentricity ( $e$ ) and longitude of periastron ( $\omega$ ) (Lange et al. 2001).

For both PSR J2145–0750 and PSR J2302+4442 we also have significant detections of Shapiro delay, requiring the use of the ELL1H model (Freire & Wex 2010), which uses an orthometric parameterization of higher order Shapiro delay harmonics. For PSR J2145–0750 we were able to measure three Shapiro delay harmonics and thus used the medium inclination case which includes the the third harmonic ( $h_3$ ) parameter

$$h_3 = r \left( \frac{s}{1 + \sqrt{1 - s^2}} \right)^3 \quad (1)$$

where  $r$  and  $s$  are the range and shape Shapiro delay parameters. We used the very high inclination parameterization for PSR J2302+4442 which includes both the  $h_3$  and the orthometric ratio ( $\varsigma$ ) parameters:

$$\varsigma = \frac{s}{1 + \sqrt{1 - s^2}} \quad (2)$$

#### 3.2. DM Modeling

Temporal DM variations were modeled using the piece-wise constant DMX model (Jones et al. 2017; Agazie et al. 2023b). In the wideband likelihood, the weighted mean of the wideband DM values in a DMX MJD range serves as the prior for fitting the DMX values (Alam et al. 2021a). Thus, if there is significant variation in the number of observations per DMX range, this may artificially weight DMX values from denser ranges. The NG15 DMX models for the sources in this paper used 6.5-day DMX ranges for GUPPI TOAs

and 15-day ranges for GASP TOAs, which were determined by the cadence of the dual frequency observations required for accurate DM measurements (Jones et al. 2017). CHIME’s wide 400 MHz bandwidth is large enough to make independent DM measurements without the presence of dual frequency observations (CHIME/Pulsar Collaboration et al. 2021).

Similarly to Fonseca et al. (2021), we tested two categories of DMX ranges: constant and hybrid. In constant range models, we used the same DMX range width (6.5 d, 15 d, 30 d) across the entire timing baseline. The only exceptions were for the two sources with GASP data (PSR J1012+5307 and PSR J2145–0750) for which ranges including GASP TOAs had a minimum 15 d length. As DMX models add a large number of parameters to the timing model, the longer DMX ranges were used to test if we may be able to sufficiently model slowly evolving DM variations with fewer parameters.

In hybrid range models we used combinations of longer DMX ranges for data prior to MJD 58600 (30 d, 15 d, 6.5 d) and shorter ranges after (15 d, 6.5 d, 3 d) to account for the higher cadence of CHIME data (Table 3). Model selection was done using the Akaike Information Criterion (AIC) statistic (Burnham & Anderson 2004). The DMX model with the lowest AIC for each source was the “preferred” model and other models were discarded if the relative likelihood ( $\exp(-\Delta\text{AIC}/2)$ ) was below 0.05 which corresponds to a  $\Delta\text{AIC}$  of roughly 6. For PSR J0645+5158 and PSR J1012+5307 the preferred DMX model was a hybrid range model with 6.5 d/3 d ranges pre/post MJD 58600. The preferred model for PSR J2302+4442 was a constant range model with 30 d bin widths. Timing results reported in Table 1 are using the preferred DMX model respective to each pulsar.

PSR J2145–0750 has two DMX models from which we cannot distinguish a preferred model with the AIC statistic alone. The hybrid 6.5 d/3 d range model technically has the lowest AIC value, but there is only a  $\Delta\text{AIC}$  of 1 with the 15 d/3 d range model. This gives us a relative likelihood of 0.6 for the 15 d/3 d model to minimize information loss compared to the the 6.5 d/3 d model. Even though the maximum DMX range for pre MJD 58600 data is more than doubled in the 15 d/3 d model, the roughly monthly cadence of observations in this period means there are only seven fewer DMX parameters than the 6.5 d/3 d model. Given the very large number of total DMX parameters in each model (445 vs. 438) these models are not different enough from each other for one to be preferred over the other. The more extreme temporal DM variations for this source are in post MJD 58600 data which has the same DMX range width for

<sup>43</sup> <https://github.com/nanograv/PINT>

both models (Fig. 1). Since neither is preferred we decided to select the 15 d/3 d model as it has slightly fewer free parameters.

### 3.3. Noise Modeling

Analysis of noise properties in the TOA and DM residuals was done using the same methodology as Alam et al. (2021a) and Agazie et al. (2023b) using the `enterprise` Bayesian pulsar timing suite (Ellis et al. 2020). Once both white and red noise parameters are determined with `enterprise`, they are included in the timing ephemeris as frozen parameters. For each receiver/backend combination, white noise was parameterized using EFAC, DMEFAC, EQUAD, and DMEQUAD. EFAC is a linear scaling factor for TOA uncertainties used to account for mismatches between the template portrait and the data, and EQUAD accounts for additive white noise and is added in quadrature to TOA uncertainties. DMEFAC and DMEQUAD are analogous to EFAC and EQUAD, but applied to the WB TOA DM measurements (Alam et al. 2021a). Red noise is modeled as a stationary Gaussian process with power spectrum:

$$P(f) = A_{\text{red}}^2 \left( \frac{f}{1\text{yr}^{-1}} \right)^{\gamma_{\text{red}}} \quad (3)$$

Where  $A_{\text{red}}$  is the power spectrum amplitude at a frequency of  $1\text{ yr}^{-1}$ ,  $f$  is the Fourier frequency, and  $\gamma_{\text{red}}$  is the spectral index. Similarly to Alam et al. (2021a) we considered detection of red noise to be significant if the Savage-Dickey density ratio of the posterior distribution of  $\log_{10}(A_{\text{red}})$  exceeded 100 (Dickey 1971). We detected significant red noise in PSR J1012+5307, which was also detected in NG15. We get somewhat different values for  $\gamma_{\text{red}}$ , but the NG15 value of  $-0.8(3)$  is consistent within the  $2\text{-}\sigma$  confidence interval of the CHIME/NG15 result of  $-1.3(4)$ . The Fourier frequencies used to fit for  $A_{\text{red}}$  and  $\gamma_{\text{red}}$  are dependent on the total timing baseline, which is longer by nearly three years for CHIME/NG15, thus we fitting these parameters using somewhat different frequencies. Additionally, the added CHIME data has both a higher observing cadence and increased TOA uncertainties, which implicitly changes the weighting of the underlying basis functions used for fitting. Both PSR J0645+5158 and PSR J2302+4442 did not have significant detections of red noise in both this analysis and NG15. For PSR J2145–0750, there was significant red noise in the NG15 data, but with the combined CHIME/NG15 dataset our attempts to model red noise would introduce large, non-physical sinusoids in our timing residuals so we excluded it from the noise model and only used white noise parameters. We believe this difficulty may be due to the strong solar wind variability

we see the DM times series (Sections 3.2 & 4.5). If we had been able to model red noise we would expect to see some increases in timing parameter uncertainty and possibly some changes in post-keplerian parameter measurements as unmodeled red noise processes would vary on similar timescales to relativistic post-keplerian processes. For PSR J1012+5307 we did observe some changes to post-keplerian parameters orbital decay and rate of change of the projected semi-major axis prior to and after introducing a red noise model that were within  $2\text{-}\sigma$  measurement uncertainties.

## 4. RESULTS

### 4.1. PSR J0645+5158

We report marginal improvement in precision of the updated timing astrometric measurements for the isolated PSR J0645+5158. Our new parallax distance of  $1.2(2)$  kpc which has  $2\text{-}\sigma$  agreement with the NG15 distance of  $1.5(3)$  kpc. Using our proper motion measurements we determined a total proper motion of  $7.62 \pm 0.02\text{ mas yr}^{-1}$  and a corresponding transverse velocity of  $45 \pm 8\text{ km s}^{-1}$ .

Our  $\dot{P}$  measurement was mostly due to intrinsic pulsar spin down ( $\dot{P}^{\text{Int}}$ ) but we did estimate significant extrinsic contributors:

$$\dot{P} = \dot{P}^{\text{Int}} + \dot{P}^{\text{Shk}} + \dot{P}^{\text{Gal,rad}} + \dot{P}^{\text{Gal,az}} \quad (4)$$

This includes the kinematic term contribution due to transverse velocity of the pulsar ( $\dot{P}^{\text{Shk}}$ ) and acceleration due to differential galactic rotation ( $\dot{P}^{\text{Gal,rad}}$ ), and acceleration towards the galactic disk ( $\dot{P}^{\text{Gal,az}}$ ) (Shklovskii 1970; Damour & Taylor 1991; Nice & Taylor 1995).

We estimated  $\dot{P}^{\text{Shk}}$  to be  $2.1(4) \times 10^{-22}\text{ ss}^{-1}$  using:

$$\dot{P}^{\text{Shk}} = P \frac{(\mu_{\alpha}^2 + \mu_{\delta}^2)D}{c} \quad (5)$$

Where  $\mu_{\alpha} \equiv \frac{d\alpha}{dt} \cos \delta$  is the proper motion in right ascension,  $\mu_{\delta}$  is the proper motion in declination, and  $D$  is the parallax distance.

We estimated  $\dot{P}^{\text{Gal,rad}}$  to be  $6.6(1.1) \times 10^{-22}\text{ ss}^{-1}$  using:

$$\dot{P}^{\text{Gal,rad}} = P \left[ \frac{-\Omega_0}{cR_0} \cos b \left( \cos l + \frac{\beta}{\beta^2 + \sin^2 l} \right) \right] \quad (6)$$

Where  $l$  and  $b$  are the Galactic coordinates of the pulsar,  $d$  is the parallactic distance, and  $\beta \equiv \frac{d}{R_0} \cos b - \cos l$ . We used a Sun-Galactic Center distance  $R_0 = 8.275 \pm 0.033\text{ kpc}$  (GRAVITY Collaboration et al. 2021) and a circular speed of the local standard of rest of  $\Omega_0 = 233.3 \pm 1.4\text{ km s}^{-1}$  (McGaugh 2018).

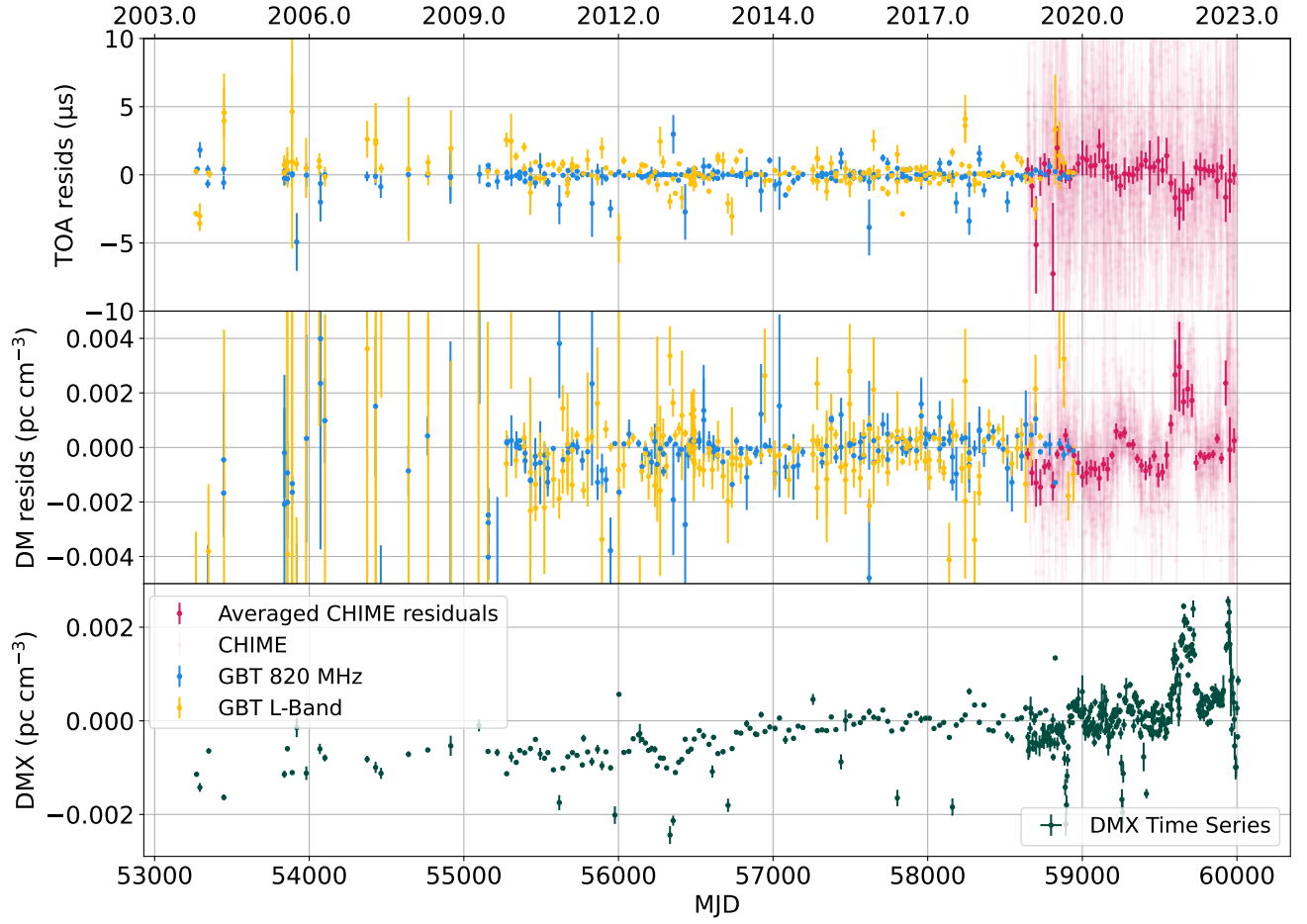


**Figure 1.** Top plot: timing residuals for PSR J2145–0750; Middle plot: DM residuals; Bottom plot: DMX time series where vertical bars indicate DMX parameter uncertainty and horizontal bars indicate the width of DMX bins in time.

**Table 3.**  $\Delta\text{AIC}$  values for each set of DMX model parameters, where  $\Delta\text{AIC} = \text{AIC} - \text{AIC}_{\min}$ . A  $\Delta\text{AIC}$  value of zero indicates the DMX model with the lowest AIC value for each source.

Model	J0645+5158	J1012+5307	J2145–0750	J2302+4442
6.5 day	36	85	856	144
15 day	71	266	2659	65
30 day	1455	1266	10649	0
6.5 day NG15 3 day CHIME	0	0	0	217
15 day NG15 3 day CHIME	9	29	1	218
15 day NG15 6.5 day CHIME	45	105	755	144
30 day NG15 3 day CHIME	97	878	2295	190
30 day NG15 6.5 day CHIME	138	1007	3108	113
30 day NG15 15 day CHIME	163	1168	5409	36

We estimated  $\dot{P}^{\text{Gal,az}}$  to be  $-4.1(4) \times 10^{-22} \text{ s s}^{-1}$  using:

$$\dot{P}^{\text{Gal,az}} = P \left[ \frac{K_z |\sin b|}{c} \right] \quad (7)$$

Where  $K_z$  is the vertical component of Galactic acceleration. We have used the approximation for  $K_z$  in Equation 17 in Lazaridis et al. (2009) which is accurate for Galactic heights  $z \equiv |d \sin b| \leq 1.5 \text{ kpc}$  (Holmberg & Flynn 2004). This source has a Galactic height of roughly  $0.43 \text{ kpc}$ .

This leaves us with a remaining intrinsic  $\dot{P}$  of  $4.5(12) \times 10^{-21} \text{ s s}^{-1}$ .

#### 4.2. PSR J1012+5307

Measurement of orbital decay ( $\dot{P}_B$ ) for PSR J1012+5307 improved in precision by a factor of five compared to the NG15 measurement of  $6.1(5) \times 10^{-14} \text{ s s}^{-1}$  (Agazie et al. 2023b). We looked at several potential intrinsic and extrinsic contributors to the observed total  $\dot{P}_B$ :

$$\dot{P}_B^{\text{Tot}} = \dot{P}_B^{\text{GR}} + \dot{P}_B^{\text{Shk}} + \dot{P}_B^{\text{Gal}} + \dot{P}_B^{\dot{m}} + \dot{P}_B^{\text{T}} + \dot{P}_B^{\text{ex}} \quad (8)$$

The emission of gravitational waves ( $\dot{P}_B^{\text{GR}}$ ), mass loss from the system ( $\dot{P}_B^{\dot{m}}$ ), and tidal dissipation of the orbit ( $\dot{P}_B^{\text{T}}$ ) are all intrinsic to the binary. Extrinsic contributors include transverse acceleration of the binary system ( $\dot{P}_B^{\text{Shk}}$ ), and acceleration due to the Galactic gravitational potential ( $\dot{P}_B^{\text{Gal}}$ ) (Damour & Taylor 1991; Nice & Taylor 1995; Shklovskii 1970). For this system  $\dot{P}_B^{\dot{m}}$  and  $\dot{P}_B^{\text{T}}$  are negligible.

The most significant contributor to  $\dot{P}_B^{\text{Tot}}$  measurement for PSR J1012+5307 was the Shklovskii term which we estimated using Equation 5 with  $\dot{P}_B$  and  $P_B$  instead of  $\dot{P}$  and  $P$  (Shklovskii 1970).

The uncertainty of  $\dot{P}_B^{\text{Shk}}$  is dominated by the timing parallax measurement which, for PSR J1012+5307, was consistent within  $1.4\sigma$  to Very Long Baseline Interferometry (VLBI) determined parallax measurements from Ding et al. (2023) (Table 4). The larger uncertainty in the CHIME/NG15 timing parallax vs VLBI parallax explains the larger uncertainty of our estimate of  $\dot{P}_B^{\text{Shk}}$ , though still consistent within  $1.1\sigma$  of the  $\dot{P}_B^{\text{Shk}}$  estimate from VLBI astrometry (Table 5).

We estimated  $\dot{P}_B^{\text{Gal}}$  using methods from Nice & Taylor (1995) and Lazaridis et al. (2009).

$$\dot{P}_B^{\text{Gal}} = \frac{A_G}{c} P_B \quad (9)$$

$A_G$  is the line of sight acceleration of the pulsar binary which we calculated with the same values of  $R_0$  and  $\Omega_0$  used in Equation 6.

**Table 4.** Astrometry comparison for J1012+5307

Analyses	$\mu_\alpha$ (mas yr <sup>-1</sup> )	$\mu_\delta$ (mas yr <sup>-1</sup> )	$\varpi$ (mas)
This work	2.620(6)	-25.529(6)	1.0(10)
Ding et al. (2020)	2.67(9)	-25.40(14)	1.21(8)
Ding et al. (2023)	2.61(1)	-25.49(1)	1.14(4)

This gave us a remaining excess  $\dot{P}_B$  term of  $-23(8) \text{ fs s}^{-1}$ . While this excess term is only marginally significant due to the high uncertainty, we hypothesized that it was likely due to  $\dot{P}_B^{\text{GR}}$ . We re-did our calculation of this excess term using the  $\dot{P}_B^{\text{Shk}}$  and  $\dot{P}_B^{\text{Gal}}$  terms calculated from VLBI astrometry and this time got a much more precise value of  $-15(3) \text{ fs s}^{-1}$ . This term is consistent with the estimated  $\dot{P}_B^{\text{GR}}$  from Ding et al. (2020) which itself was made using the pulsar-companion mass ratio reported in Mata Sánchez et al. (2020) and Equation 21 in Lazaridis et al. (2009).

We then treated the VLBI corrected excess  $\dot{P}_B$  term as a  $\dot{P}_B^{\text{GR}}$  estimate and looked at the implied curve in pulsar and companion mass space (Fig. 2). The  $1\text{-}\sigma$  region directly overlaps with intersection of the companion mass and pulsar-companion mass ratio curves calculated from measurements reported in Mata Sánchez et al. (2020).

The measurement of rate of change of the projected semi-major axis ( $\dot{x}$ ) for PSR J1012+5307 improved in precision by a factor of three from the NG15 value. Using our own measurement uncertainty, the NG15 value is 5 standard deviations from our measurement, suggesting the values may be significantly different, but when using the larger NG15 measurement uncertainty, our measurement was within two standard deviations. Thus we can treat these measurements as broadly consistent, with the CHIME/NG15 measurement having improved precision due to the longer timing baseline. Contributors to the measured value of  $\dot{x}$  are summarized below:

$$\dot{x}^{\text{Tot}} = \dot{x}^{\text{GR}} + \dot{x}^{\text{PM}} + \frac{d\epsilon_A}{dt} - \frac{\dot{D}}{D} + \dot{x}^{\dot{m}} + \dot{x}^{\text{SO}} + \dot{x}^{\text{planet}} \quad (10)$$

Here  $\dot{x}^{\text{GR}}$  is contribution due to the emission of gravitational waves,  $\dot{x}^{\text{PM}}$  is from proper motion of the binary system,  $\frac{d\epsilon_A}{dt}$  is varying aberration due to geodetic precession of the pulsar spin axis, and  $\frac{\dot{D}}{D}$  is changing Doppler shift.  $\dot{x}^{\dot{m}}$  is from mass loss of the system,  $\dot{x}^{\text{SO}}$  is from spin-orbit coupling, and  $\dot{x}^{\text{planet}}$  in cases of a third companion.

Our  $\dot{x}$  measurement was dominated by  $\dot{x}^{\text{PM}}$ . As all other estimated contributions are significantly smaller than the measurement uncertainty, we treated our timing measurement of  $\dot{x}$  as an upper limit for the  $\dot{x}^{\text{PM}}$  contribution. We used this to look at the combinations

**Table 5.**  $\dot{P}_B$  contributor comparison for J1012+5307. Single asterisk indicates measurement carried over from Ding et al. (2020). Double asterick indicates measurement carried over from Ding et al. (2023). As VLBI distances are more precise and reliable than those determined by pulsar timing we also calculated contributions to our  $\dot{P}_B^{\text{Tot}}$  measurement using VLBI-determined parallax and proper motion terms.

Analyses	$\dot{P}_B^{\text{Tot}}$ (fs s <sup>-1</sup> )	$\dot{P}_B^{\text{Shk}}$ (fs s <sup>-1</sup> )	$\dot{P}_B^{\text{Gal}}$ (fs s <sup>-1</sup> )	$\dot{P}_B^{\text{GR}}$ (fs s <sup>-1</sup> )	$\dot{P}_B^{\text{ex}}$ (fs s <sup>-1</sup> )
This work	53(1)	82(8)	-5.8(3)	-23(8)	
This work - VLBI corrections	53(1)	73(3)**	-4.1(4)**	-15(3)	
Ding et al. (2020)	61(4) <sup>a</sup>	68.6(4.4)	-5.5(2)	-13(1)	10.6(6.1)
Ding et al. (2023)	61(4) <sup>a</sup>	73(3)	-4.1(4)	-13(1)*	-7.9(5.0)

<sup>a</sup>Desvignes et al. (2016)

of the longitude of ascending node ( $\Omega_{\text{asc}}$ ) and the orbital inclination ( $i$ ) implied by this  $\dot{x}^{\text{PM}}$  estimate and found they are partially consistent with the  $i = 50^\circ \pm 2^\circ$  measurement reported in Mata Sánchez et al. (2020). When making no assumptions about which quadrant of  $i$  and  $\Omega_{\text{asc}}$  is correct, we found that in the  $90 - 180^\circ$  quadrant,  $i$  must be above  $120^\circ$  (Fig. 3).

We calculated more direct constraints on  $i$  in the  $0 - 90^\circ$  quadrant from the following limit (Lorimer & Kramer 2012; Kopeikin 1996):

$$\tan i \leq 1.54 \times 10^{-16} \left( \frac{\mu^{\text{T}}}{\text{mas yr}^{-1}} \right) \left( \frac{x}{\dot{x}^{\text{PM}}} \right)_{\text{max}} \quad (11)$$

From this we calculated the upper limit  $\tan i \leq 1.19(9)$ . In the  $0 - 90^\circ$  quadrant, this gave a limit of  $i \leq 52^\circ \pm 4^\circ$ . Although we treated this estimate as a limit and not a measurement of  $i$ , as this method of estimation does not constrain the longitude of ascending node, we noted that it is still consistent within  $1-\sigma$  of the Mata Sánchez et al. (2020)  $i$  measurement. We used the binary mass function to plot the combinations of pulsar and companion masses implied by our  $i$  limit in Figure 2. We showed intersection with the contours for  $q$ ,  $m_c$ , and  $\dot{P}_B$  over a pulsar mass range of  $1.3 - 2.1 M_\odot$  which is broadly consistent with the literature measurement of  $1.72 \pm 0.16 M_\odot$  (Mata Sánchez et al. 2020).

### 4.3. PSR J2145–0750

Our detection of the  $h_3$  Shapiro delay parameter is not sufficient to directly determine  $m_c$  and  $\sin i$ , as we could not detect any higher harmonics. Instead we defined a curve in  $m_c$  and  $\sin i$  space implied by our  $h_3$  measurement using Eq. 1 (Fig. 4). We compared to results from Deller et al. (2016), which used a combination of VLBI observations and optical photometry of the WD companion to determine companion mass, inclination, and distance. As shown in Figure 4 the intersection in  $m_c - \sin i$  space is consistent within the  $1-\sigma$  error region of our  $h_3$  measurement.

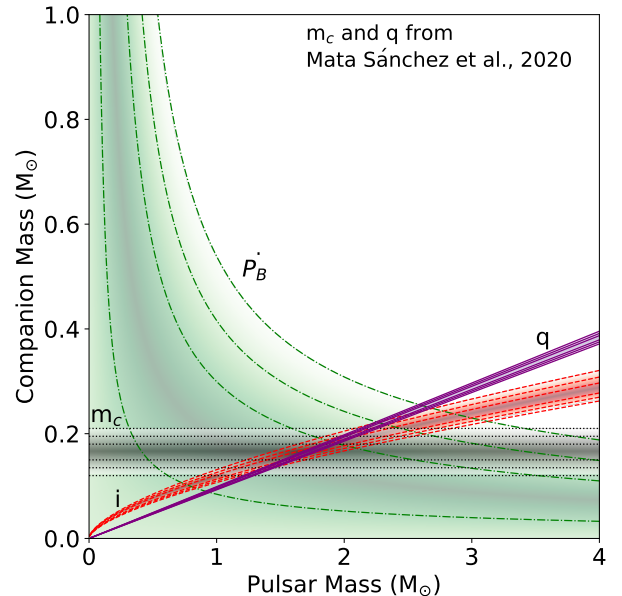


**Figure 2.** Pulsar and companion mass constraints for PSR J1012+5307. Green contours are from the estimated  $\dot{P}_B^{\text{GR}}$  term and red contours are from inclination angle constraint determined from the kinematic term of  $\dot{x}$ . Both the companion mass ( $m_c$ ) and pulsar-companion mass ratio ( $q$ ) contours are determined from measurements from Mata Sánchez et al. (2020)

The CHIME/NG15  $\dot{x}$  measurement improved in precision by a factor of 4 from the NG15 measurement, but has changed in value and is  $12.5-\sigma$  from the NG15 value of (Agazie et al. 2023b). Looking at other analyses of this pulsar, such as Reardon et al. (2021) and Perera et al. (2019), our  $\dot{x}$  is more precise but has significantly increased (Table 6). Our analysis uses a much longer timing baseline than both Agazie et al. (2023b) and Reardon et al. (2021), which may explain the improved precision from these two analyses. It is possible that since we were unable to model red noise, which has been significantly detected in this source in previous analyses and can impact post-keplerian parameters if unmodeled,

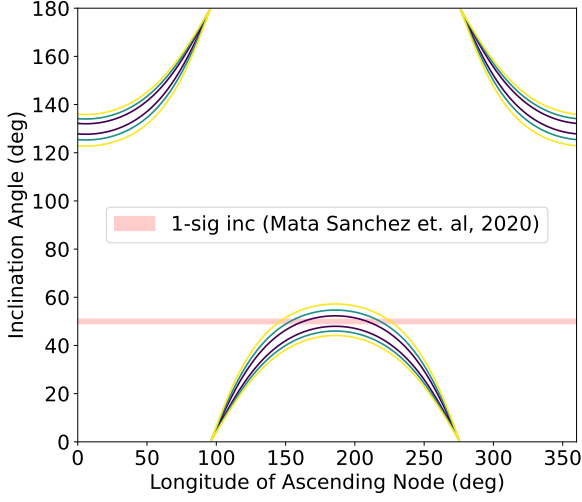


**Figure 3.** Contours of  $\Omega_{\text{asc}}$  and  $i$  from  $\dot{x}$  measurement for J1012+5307

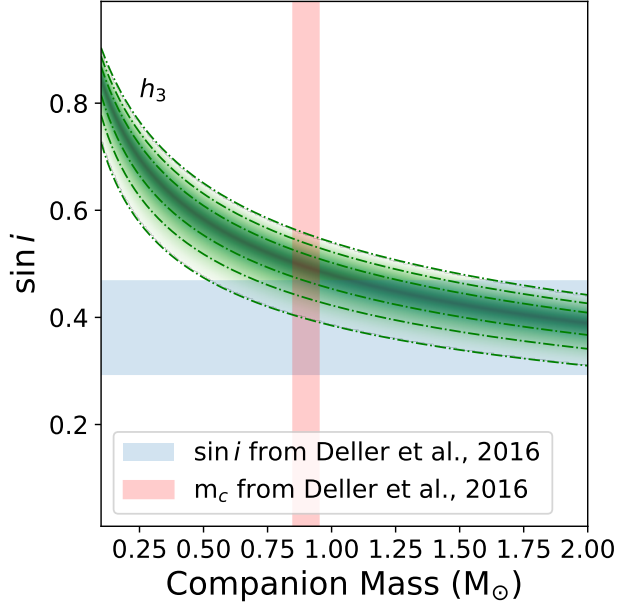


**Figure 4.** In green, the curve of  $m_c$  vs  $\sin i$  from detected value of  $h_3$  for PSR J2145–0750. The dashed lines represent the 1, 2, and 3- $\sigma$  error regions. Red and blue shaded region represent the 1- $\sigma$  range of  $m_c$  and  $\sin i$  measurements respectively from Deller et al. (2016)

this maybe the reason we detect a significantly higher  $\dot{x}$  value. Similarly to PSR J1012+5307, the  $\dot{x}$  measurement for PSR J2145–0750 is dominated by the  $\dot{x}^{\text{PM}}$  term and all other estimated contributors are smaller than the measurement uncertainty. Using the same methods as in Section 4.2, we show that the implied

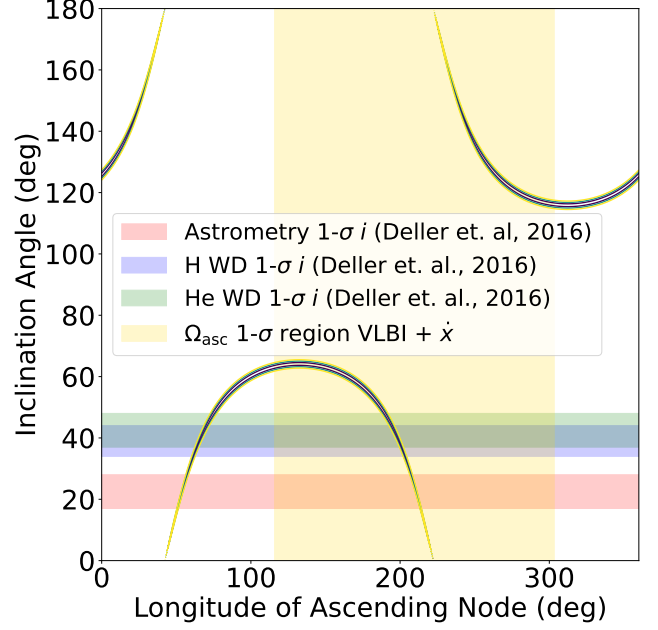


**Figure 5.** Contours of  $\Omega_{\text{asc}}$  and  $i$  calculated from  $\dot{x}$  measurement of PSR J2145–0750. The gold region represent the 1- $\sigma$  error region of  $\Omega_{\text{asc}}$  determined by calculation of reflex motion of VLBI data using our  $\dot{x}$  measurement as a prior.

combinations of  $i$  and  $\Omega_{\text{asc}}$  broadly overlap within the  $0^\circ$ – $90^\circ$   $i$  quadrant with VLBI determined measurements from Deller et al. (2016) of  $i$  (Fig. 5). Again using Equation 11 we calculated an upper limit of  $\tan i \leq 1.98(4)$  which corresponds to an  $i$  limit of  $63(4)^\circ$  in the  $0^\circ$ – $90^\circ$   $i$  quadrant.

#### 4.4. PSR J2302+4442

PSR J2302+4442 has a significant detection of Shapiro delay from which we determined the companion and pulsar masses, as well as the system inclination. To determine robust credible intervals for  $m_c$ ,  $m_p$ , and  $i$ , we used the  $\chi^2$  gridding method described in Splaver et al. (2002). We started with a range of values from uniform distributions of  $m_c$  and  $\cos i$  and then calculated corresponding values of  $h_3$  and  $\zeta$  using equations 1 and 2. These  $h_3$  and  $\zeta$  pairs are then inserted in the timing model as frozen parameters and the timing model is re-fit with all other free parameters allowed to vary and the  $\chi^2$  recorded. This  $\chi^2$  grid is then mapped into the following likelihood function where  $\chi_0^2$  is the minimum  $\chi^2$ :

$$p(h_3, \zeta | \text{data}) = \exp\left(-\frac{(\chi^2 - \chi_0^2)}{2}\right) \quad (12)$$

Using Bayes’s theorem and equations 1 and 2 we can then transform this likelihood into a posterior PDF for  $m_c$  and  $\cos i$ :

**Table 6.** Astrometry comparison for PSR J2145–0750, with last digit uncertainties in parentheses. Red text indicates values reported without measurement uncertainties.

Analyses	$\mu_\alpha$ (mas yr <sup>-1</sup> )	$\mu_\delta$ (mas yr <sup>-1</sup> )	$\varpi$ (mas)	$\dot{x}$ (10 <sup>-15</sup> ls s <sup>-1</sup> )
This work	-9.71(11)	-8.54(4)	1.55(5)	10.2(2)
Agazie et al. (2023b)	-9.54(4)	-8.9(17)	1.5(18)	7.5(8)
Reardon et al. (2021)	-9.48(2)	-9.11(7)	1.40(8)	6.1(4)
Deller et al. (2016)	-9.46(5)	-9.08(6)	1.63(4)	...
Perera et al. (2019)	-9.58(3)	-8.87(7)	1.54(10)	7.5(5)
Miles et al. (2023)	-9.46	-8.08	1.33	-35(5)
Shamohammadi et al. (2024)	-9.7(3)	-8.2(10)	1.6(3)	...

$$p(m_c, \cos i | \text{data}) = \left| \frac{\partial h_3}{\partial m_c} \frac{\partial \varsigma}{\partial \cos i} \right| p(h_3, \varsigma | \text{data}) \quad (13)$$

We can then use the Keplerian mass function to translate this into a 2D-PDF for  $m_p$  and  $\cos i$ .

$$p(m_p, \cos i | \text{data}) = \left| \frac{\partial m_c}{\partial m_p} \right| p(m_c, \cos i | \text{data}) \quad (14)$$

We determined confidence intervals for  $m_c$ ,  $m_p$ , and  $\cos i$  by marginalizing each of the 2-D PDFs over one variable to get the 1-D PDFs of the corresponding variable (Fig. 6 and 7). For  $m_c$  we got  $0.35^{+0.05}_{-0.04} M_\odot$ ,  $m_p$  was  $1.8^{+0.3}_{-0.3} M_\odot$ , and  $\cos i$  was  $0.17^{+0.03}_{-0.02}$  which corresponds to an inclination angle of  $80^{+1}_{-2}$ .

Comparing this result to the NG15 Shapiro delay results, we switched the binary model from DD to ELL1H due to the nearly circular eccentricity, and thus used a different parameterization. In the DD binary model, Shapiro delay is parameterized in the timing model by  $m_c$  and  $\sin i$  (Damour & Deruelle 1985, 1986). The combined CHIME/NG15 results show significant improvement from the Shapiro-delay estimated mass measurements from Agazie et al. (2023b), which reported an  $m_c$  of  $0.3 \pm 0.1 M_\odot$ ,  $m_p$  of  $5.2^{+3.0}_{-3.2} M_\odot$ , and system inclination of  $78^\circ \pm 3.3^\circ$ . Our results for  $m_c$  and  $i$  have improved precision by a factor of 2 and are consistent within the 1- $\sigma$  error region. Our  $m_p$  measurement uncertainty is dramatically lower by two orders of magnitude and is well-determined in a more physically motivated range of pulsar masses than the analysis in Agazie et al. (2023b). This improvement is possibly due to a combination of the longer timing baseline having more full orbits, this pulsar has a long binary period of 125 days, and the change to the ELL1H binary model to account for the nearly circular orbit and high system inclination.

#### 4.5. Solar wind modeling

The solar wind is typically modeled in pulsar timing as a spherical distribution of free electrons that is constant

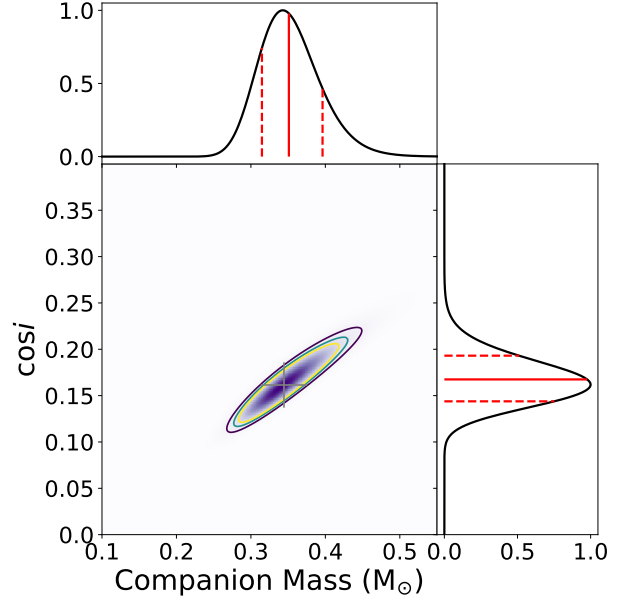


**Figure 6.** PSR J2302+4442 measurement of companion mass and cosine of inclination ( $\cos i$ ) from Shapiro delay. Center plot is the 2-D posterior pdf in purple for  $m_c$  and  $\cos i$  with 1,2,3- $\sigma$  contours overlaid. The grey cross in the center is the analytically determined 68% confidence intervals for  $m_c$  and  $\cos i$ . Top plot is the marginalized 1-D PDF for  $m_c$ , and right side plot is the marginalized 1-D PDF for  $\cos i$ . Solid red lines indicate the measurement value, and dotted red lines indicate bounds of the 68% confidence intervals.

in time. In the timing model it is parameterized with a solar wind electron density ( $n_e$ ) parameter and a radial power law index (Edwards et al. 2006). DM variations from this model can be calculated as follows:

$$DM_{SW} = n_e (1\text{AU})^2 \frac{\theta}{r_e \sin \theta} \quad (15)$$

Where  $n_e$  is the solar wind electron density at 1 AU,  $r_e$  is the Earth-Sun distance, and  $\theta$  is the pulsar-Sun-observatory angle. In low ecliptic latitude pulsars, these DM variations can be visible in the DM time series as annual peaks that correspond to a minimized solar angle

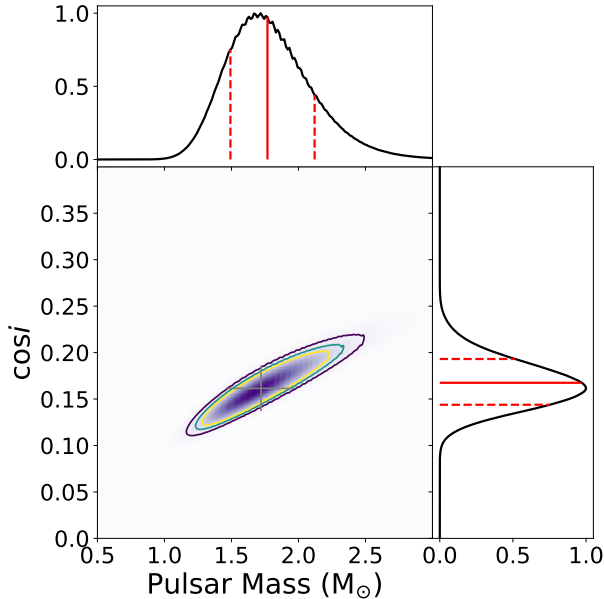


**Figure 7.** PSR J2302+4442 pulsar mass constraints from Shapiro delay measurement. Center plot is the 2-D posterior pdf in purple for  $m_p$  and  $\cos i$  with 1,2,3- $\sigma$  contours overlaid. The grey cross in the center is the analytically determined 68% confidence intervals for  $m_p$  and  $\cos i$ . Top plot is the marginalized 1-D PDF for  $m_p$ , and right side plot is the marginalized 1-D PDF for  $\cos i$ . Solid red lines indicate the measurement value, and dotted red lines indicate bounds of the 68% confidence intervals. Jagged line in the top plot is an artifact of the interpolator used for plotting.

(Tiburzi et al. 2019). This effect is particularly well-illustrated in the CHIME era data for PSR J2145–0750 (Fig. 8).

Many previous studies have demonstrated that the radial model is insufficient to precisely model  $DM_{SW}$  variations on both long and short timescales (You et al. 2012; Tiburzi et al. 2019; Hazboun et al. 2022). For PSR J2145–0750, we noticed that the DMX time series doesn’t show constant amplitudes of the  $DM_{SW}$  peaks, and that the peaks are not symmetrical, nor consistent with a radial power law fall off. As seen in Figure 8, the solar wind peaks have a much shallower slope than we would expect with the radial model.

We tried several methods of modeling the SW. When using the standard radial model, we found it to be highly covariant with the DMX model, and observed sharp dips in the DMX time series points that corresponded to conjunction. We also tried the `pint SolarWindDispersionX` model, which is a piece-wise constant representation of the solar wind density parameterized by a maximum solar wind DM at conjunction and a power-law index (Susobhanan et al. 2024). This

model assumes that the excess solar wind DM is zero at opposition. We used a single SWX bin for data prior to MJD 58600 as the detected excess  $DM_{SW}$  was relatively low and not significantly different from one year to the next. For data after MJD 58600 we used one SWX bin per year. We found that this model was unable to capture the asymmetry in the SW peaks and still left significant SW-like structure in our DMX time series and WB DM residuals. For our analysis, we found the simplest and most robust method of modeling all the  $DM_{SW}$  variations was to use more dense DMX binning for data post MJD 58600. This alternative method still did not entirely eliminate solar wind-like structure from the DM residuals for this source as shown in Figure 1. One of the largest SW peaks in 2022 also corresponds to a dip in the TOA residuals. In future analyses, the CHIME data for this system could be used to test more complex solar wind models that can better separate ISM contribution to DM vs solar wind contribution.

## 5. DISCUSSION

The combination of four years of CHIME data with NG15 data have already massively increased the TOA volume per source. Even for sources like PSR J1012+5307 and PSR J2145–0750 that have the longest NG15 timing baseline, there are already enough CHIME TOAs to nearly triple the total TOA volume (Table 1). This increase will get compounded in narrow-band datasets made with CHIME data as there could be anywhere from several to dozens of TOAs per observations to allow proper frequency coverage. For comparison, in NG15 the narrowband datasets for the sources in this paper had at least 41 times the number of TOAs as the corresponding NG15 WB datasets. As CHIME data is currently being incorporated into multiple upcoming PTA datasets, such as NANOGrav’s upcoming 20-year dataset and IPTA’s third data release, this sudden explosion of TOAs is likely to create a data volume issue for both single source analyses and PTA analyses.

### 5.1. PK parameter improvements

The fractional uncertainty of PK parameters is expected to decrease with increasing observing baseline. The  $\dot{P}_B$  measurement for PSR J1012+5307 decreased in fractional uncertainty between the 12.5 yr dataset and NG15 by the theoretical expected improvement of  $T^{-5/2}$  (Damour & Taylor 1992; Alam et al. 2021a; Agazie et al. 2023b), where  $T$  represents the observing time in years. Similarly the improvement in fractional uncertainty with the inclusion of four years of CHIME data to NG15 was also  $T^{-5/2}$ . We also calculated that the fractional uncertainty of  $\dot{x}$  for PSR J1012+5307 improved by roughly

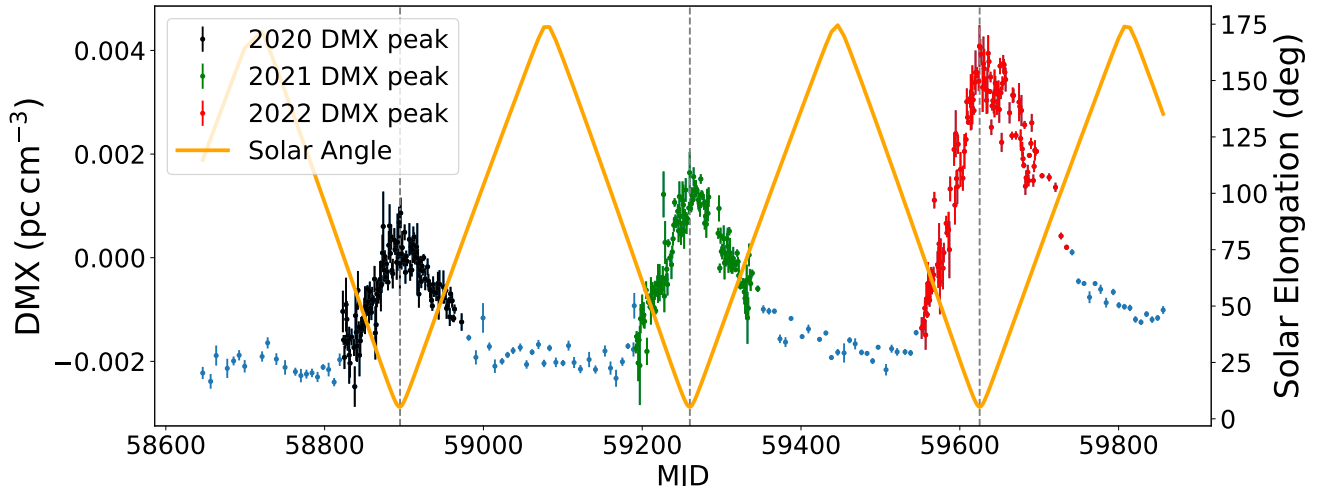


**Figure 8.** Partial DMX time series for CHIME-era PSR J2145–0750 data. The gold line indicates solar angle and the dotted grey lines represent each annual conjunction. The DMX points corresponding to bins where we detect excess solar wind DM are color coded by year.

$T^{-2.1}$  between NG15 and our CHIME/NG15 analysis. This parameter was newly detected for this source NG15 so we could not compare to the 12.5 yr dataset. We were able to do a comparison for the  $\dot{x}$  measurement for PSR J2145–0750, where the 12.5-yr to NG15 improvement was  $T^{-2.3}$  and the NG15 to CHIME/NG15 improvement was  $T^{-2.2}$ . These very similar improvements in fractional uncertainty likely indicate that the higher cadence of the CHIME data is less important for the improvement of PK parameter measurements. The inclusion of CHIME data mainly benefits these PK measurements by significantly increasing the timing baseline.

### 5.2. CHIME Frequency coverage and WB TOA precision

In nearly all of the timing residual plots it is clear that the CHIME WB TOAs, on average, have larger uncertainties compared to many of the NG15 WB TOAs (Figs 9, 10, 1, 11). Some of this increase can be attributed to CHIME operating at lower frequencies than nearly all the receivers used for NG15. TOA uncertainty scales as  $\nu^{-1/2}$ , so we would generally expect high-frequency TOAs to have smaller error bars. The CHIME telescope also has a lower gain, which is inversely proportional to TOA uncertainty, than the GBT (Lorimer 2008; Lorimer & Kramer 2012).

The corresponding WB DMs are the opposite, with the CHIME WB DMs being much more precise than GUPPI or GASP DMs. This decrease is likely due to CHIME’s frequency coverage being larger and covering lower frequencies than any of the GBT receivers used.

DM is measured by the delay between pulse arrivals from different frequencies. Lower frequencies will have a much larger lever arm on measuring DM delay, which scales with  $\nu^{-2}$ . Using PSR J0645+5158 as an example, the DM delay across the CHIME bandwidth was 291 ms, whereas the delay across the 820 MHz receiver was 43 ms and the delay across the L-Band receiver would only be 29 ms. ISM propagation effects are a significant source of noise for PTA analyses, so the increase in total observing range due to the inclusion of low-frequency, high precision, CHIME DM data will be important for modeling frequency-dependent DMs (Agazie et al. 2023c). The high cadence observing also is beneficial for monitoring short and long timescale DM fluctuations.

Our RFI excision approach to remove bad channels after frequency and time averaging has the potential to cause us to lose a significant percentage of frequency information. When constructing the data portraits we scrunched in frequency to 64 bins and kept 53% of frequency coverage for PSR J0645+5158, 68% for PSR J1012+5307, 57% for J2145–0750, and 40% for PSR J2302+4442. Another compounding factor is that parts of the CHIME observing band are unprotected for radio astronomy as they overlap with frequencies used for cell phones. Thus, CHIME has an extremely variable RFI environment and continuing work is underway to develop more sophisticated automated RFI excision algorithms.

## 6. CONCLUSIONS

In this paper we presented timing results from a sample of four MSPs from the NANOGrav 15-yr dataset

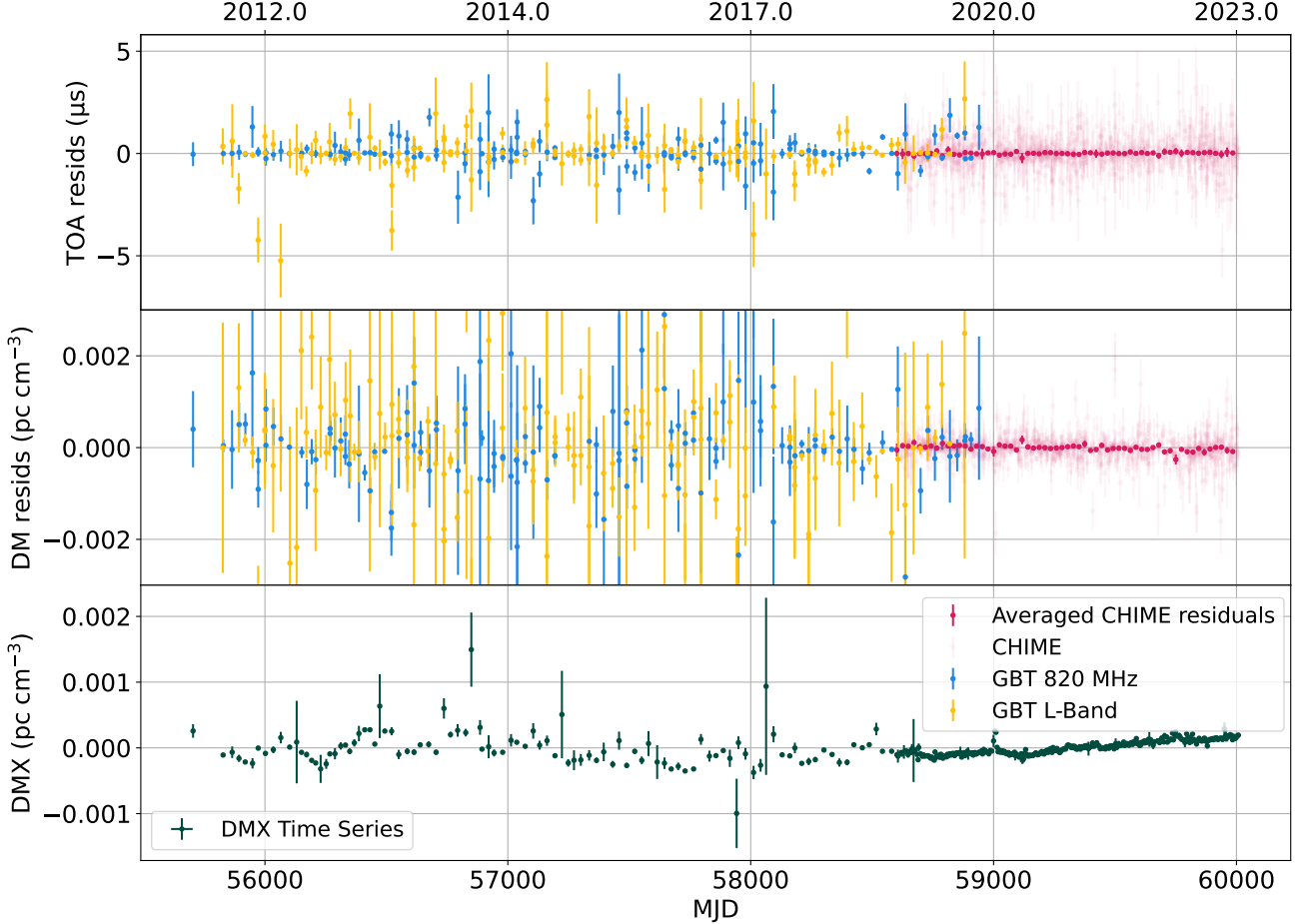


**Figure 9.** Top plot: TOA residuals for PSR J0645+5158; Middle plot: WB DM residuals; Bottom plot: DMX time series where vertical bars indicate DMX parameter uncertainty and horizontal bars indicate the width of DMX bins in time.

that have been combined with four years of daily cadence CHIME data. This is one of the first large scale efforts to include CHIME data in PTA datasets in the wideband paradigm. We summarize our major results and conclusions below.

We report significant Shapiro-delay estimated mass constraints for PSR J2302+4442. We measured a system inclination of  $80^{+1}_{-2}$ , a companion mass of  $0.35^{+0.05}_{-0.04} M_{\odot}$ , and a pulsar mass of  $1.8^{+0.3}_{-0.3} M_{\odot}$ . These measurements have not only significantly improved from the reported NG15 values, but also from those reported on optical analyses of the white dwarf companion (Kirichenko et al. 2018).

Using the proper motion and galactic acceleration derived corrections to the measured spin down of PSR J0645+5158 we get an intrinsic spindown of  $4.5(12) \times 10^{-21} \text{ s s}^{-1}$ . The significance of astrometric parameter measurements for PSR J0645+5158 improved slightly with the inclusion of CHIME data.

We report improved pulsar and companion mass constraints for PSR J1012+5307 and PSR J2145–0750 using a combination of improved PK parameter measurements and VLBI results. Measurements of post-Keplerian parameters  $\dot{P}_B$  and  $\dot{x}$  improved with the inclusion of a longer timing baseline, but don't appear significantly impacted by the higher cadence of observing. The use of CHIME data to produce more precise  $\dot{P}_B$  measurements combined with improved pulsar distances can also benefit studies of local galactic potential gradients through improved pulsar binary line of sight acceleration estimates (Moran et al. 2023, 2024).

As PTAs become more sensitive, with both longer timing datasets and increased observing bandwidths, the potential for future detection of continuous waves from individual supermassive black hole binaries will grow. The inclusion of CHIME data in PTA datasets is particularly important for studying interstellar propagation effects which can significantly impact PTA sensitivity. In future NANOGrav datasets, CHIME data will help

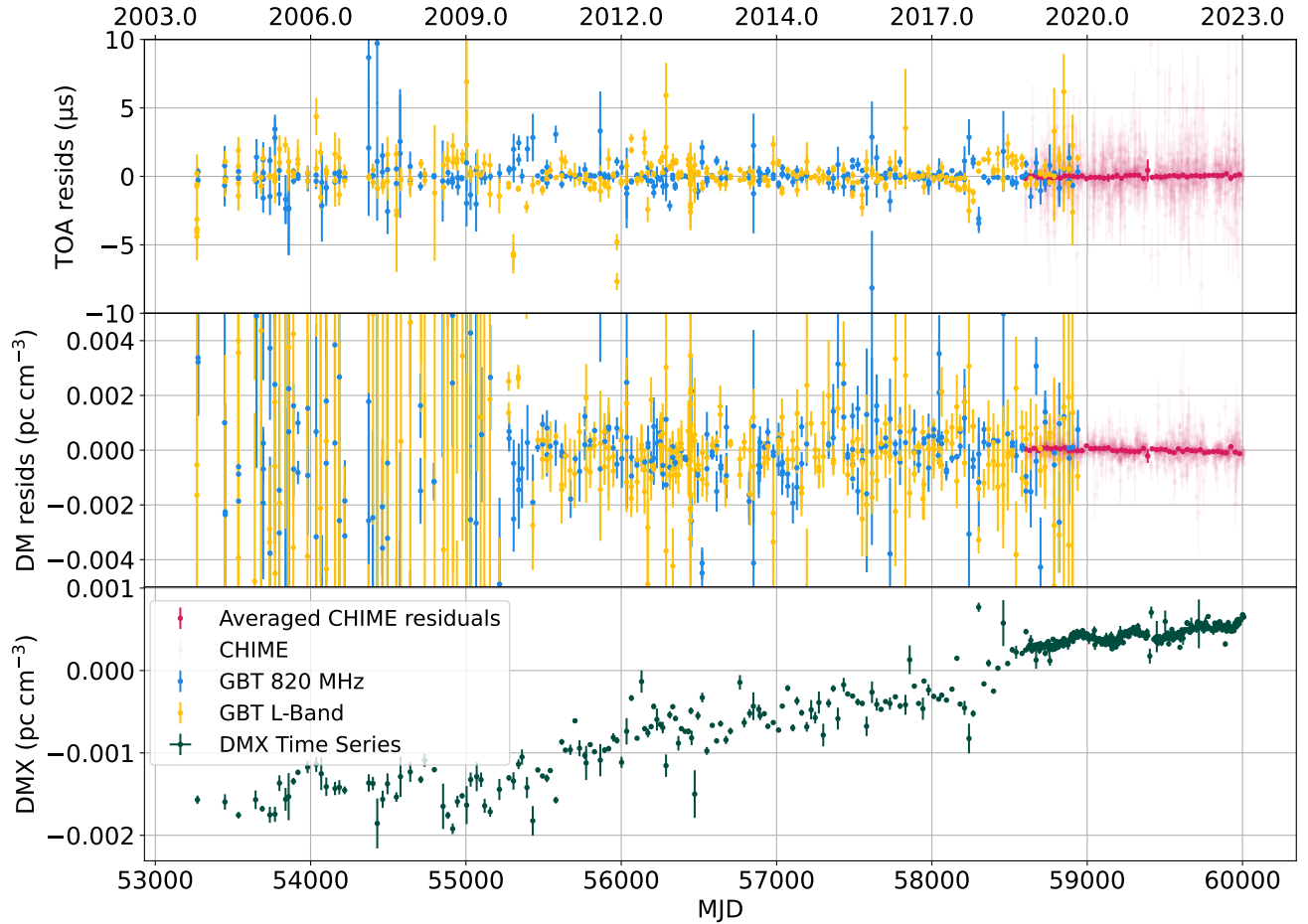


**Figure 10.** Top plot: TOA residuals for PSR J1012+5307; Middle plot: WB DM residuals; Bottom plot: DMX time series where vertical bars indicate DMX parameter uncertainty and horizontal bars indicate the width of DMX bins in time.

mitigate the loss of low-frequency observing due to the collapse of the Arecibo Telescope. CHIME WB DM data also presents a unique laboratory for studying the effect of the solar wind on pulsar timing. The more precise WB DM measurements we get from the low-frequency, high cadence CHIME data are extremely useful for illustrating short time scale ISM fluctuations, particularly DM variability from the solar wind. This was particularly well-demonstrated in the DM data for PSR J2145–0750. In future analyses CHIME data could be used to build more precise global solar wind models.

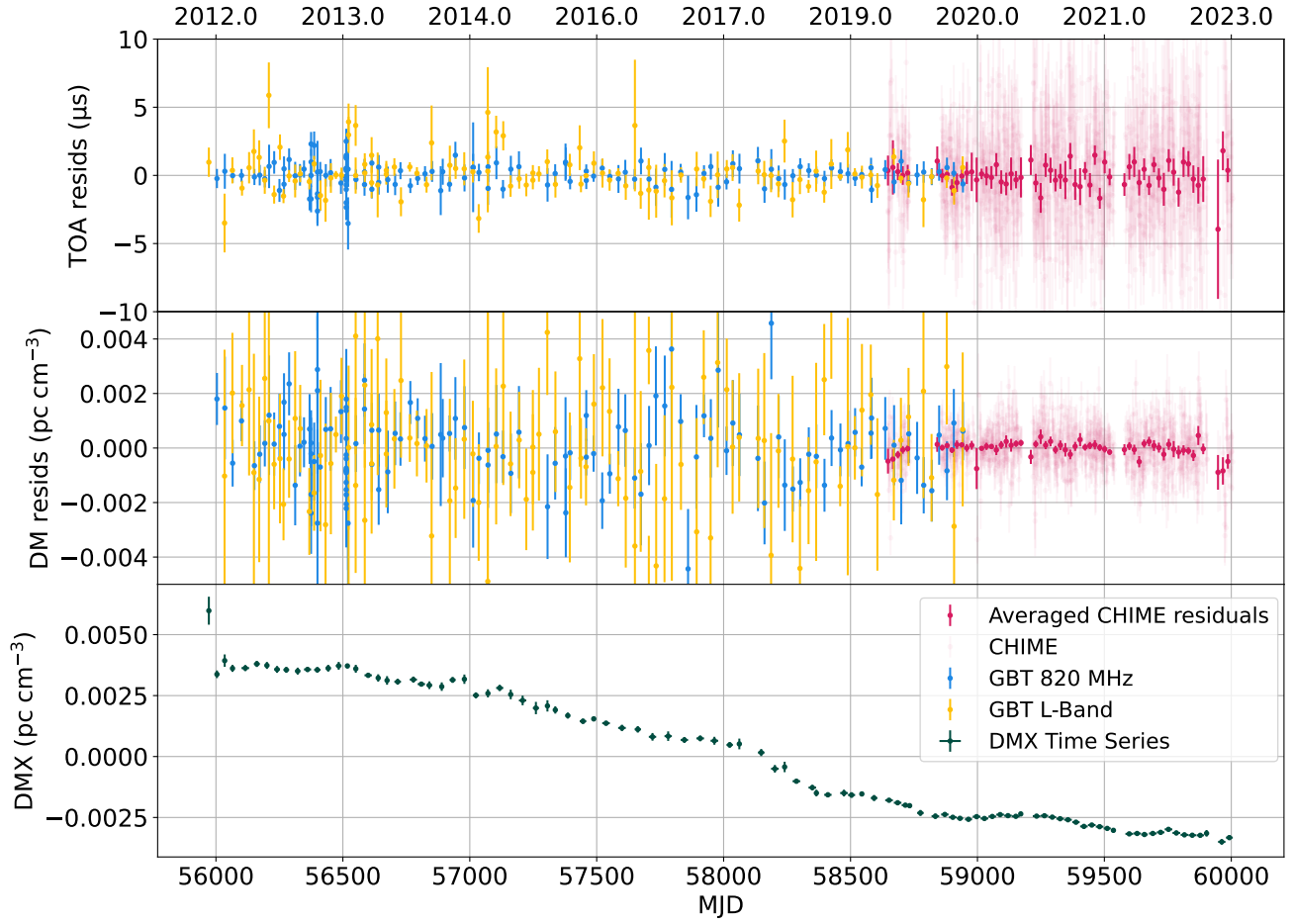


**Figure 11.** Top plot: timing residuals for PSR J2302+4442; Middle plot: DM residuals; Bottom plot: DMX time series where vertical bars indicate DMX parameter uncertainty and horizontal bars indicate the width of DMX bins in time.

This work has been carried out as part of the NANOGrav collaboration, which receives support from the National Science Foundation (NSF) Physics Frontiers Center award numbers 1430284 and 2020265. G.Y.A. was supported in part by NASA under Award Nos. RFP22.1-0 and RFP23.1-0 through the Wisconsin Space Grant Consortium Graduate and Professional Research Fellowship. P.R.B. is supported by the Science and Technology Facilities Council, grant number ST/W000946/1. H.T.C. acknowledges funding from the U.S. Naval Research Laboratory. Pulsar research at UBC is supported by an NSERC Discovery Grant and by CIFAR. K.C. is supported by a UBC Four Year Fellowship (6456). F.A.D. is supported by an NRAO Jansky fellowship. M.E.D. acknowledges support from the Naval Research Laboratory by NASA under contract S-15633Y. T.D. and M.T.L. received support by an NSF Astronomy and Astrophysics Grant (AAG) award number 2009468 during this work. E.C.F. is supported by NASA under award number 80GSFC24M0006. D.C.G. is supported by NSF Astronomy and Astrophysics Grant (AAG) award #2406919. D.R.L. and M.A.M. are supported by NSF #1458952. M.A.M. is supported by NSF #2009425. The Dunlap Institute is funded by an endowment established by the David Dunlap family and the University of Toronto. T.T.P. acknowledges support from the Extragalactic Astrophysics Research Group at Eötvös Loránd University, funded by the Eötvös Loránd Research Network (ELKH), which was used during the development of this research. H.A.R. is supported by NSF Partnerships for Research and Education in Physics (PREP) award No. 2216793. S.M.R. and I.H.S. are CIFAR Fellows. Portions of this work performed at NRL were supported by ONR 6.1 basic research funding.

The National Radio Astronomy Observatory and Green Bank Observatory are facilities of the National

Science Foundation operated under cooperative agreement by Associated Universities, Inc.

We acknowledge that CHIME is located on the traditional, ancestral, and unceded territory of the Syilx/Okanagan people. We are grateful to the staff of the Dominion Radio Astrophysical Observatory, which is operated by the National Research Council of Canada. CHIME is funded by a grant from the Canada Foundation for Innovation (CFI) 2012 Leading Edge Fund (Project 31170) and by contributions from the provinces of British Columbia, Québec and Ontario. The CHIME/FRB Project, which enabled development in common with the CHIME/Pulsar instrument, is funded by a grant from the CFI 2015 Innovation Fund (Project 33213) and by contributions from the provinces of British Columbia and Québec, and by the Dunlap Institute for Astronomy and Astrophysics at the University of Toronto. Additional support was provided by the Canadian Institute for Advanced Research (CIFAR), McGill University and the McGill Space Institute thanks to the Trottier Family Foundation, and the University of British Columbia. The CHIME/Pulsar instrument hardware was funded by NSERC RTI-1 grant EQPEQ 458893-2014.

This research was enabled in part by support provided by the BC Digital Research Infrastructure Group and the Digital Research Alliance of Canada ([alliancecan.ca](http://alliancecan.ca)).

*Facilities:* Green Bank Observatory (GBO), Dominion Radio Astrophysical Observatory

*Software:* PINT (Luo et al. 2021; Susobhanan et al. 2024), *PulsePortraiture* (Pennucci 2019), *enterprise* (Ellis et al. 2020), Matplotlib (Hunter 2007), Numpy (Harris et al. 2020), This work made use of Astropy:<sup>44</sup> a community-developed core Python package and an ecosystem of tools and resources for astronomy (Astropy Collaboration et al. 2013, 2018, 2022).

## APPENDIX

### A. THE CHIMERA PIPELINE

We developed the `chimera` pipeline<sup>45</sup> to measure wideband TOAs from the partially folded profiles in the `Timer` format generated by the CHIME/Pulsar backend (Susobhanan 2026). `chimera` is written in Python and provides a command-line script named `chimerawb`<sup>46</sup>. The `chimerawb` command takes an input directory containing `Timer` archives (van Straten & Bailes 2011), a configuration file in the JSON format, optionally a meta file containing the list of input archives to be processed, and an output directory as input, and writes a `tim` file containing wideband TOAs in the IPTA format into the output directory. The configuration file contains information about the pulsar name,

<sup>44</sup> <http://www.astropy.org>

<sup>45</sup> Available at <https://doi.org/10.5281/zenodo.18458818>.

<sup>46</sup> `chimera` is written with a structure similar to and reuses code from the `pinta` pipeline of the Indian Pulsar Timing Array (Susobhanan et al. 2021).

fiducial DM, template portrait, number of subintegrations/channels for time/frequency scrunching, and a list of bad channels for pulsar-specific RFI flagging. The template portrait is generated manually beforehand using the `ppspline` command of `PulsePortraiture` from an epoch-averaged profile obtained from multiple observations, since individual CHIME observations may have low S/N (Pennucci 2019); see section 2.4. The TOAs are generated using the `pptoa` command of `PulsePortraiture` (Pennucci 2019).

The specific operations performed by the `chimerawb` command are listed below:

1. For each `Timer` file in input directory:
  - (a) Perform automated RFI flagging.
  - (b) Convert from `Timer` to PSRFITS format (Hotan et al. 2004).
  - (c) Scrunch in time and frequency.
  - (d) Perform pulsar-specific RFI flagging using the given list of bad channels.
2. Generate wideband TOAs and save them as a `tim` file.

An example invocation of `chimerawb` is given below:

```
$ chimerawb -i J1234+5678_data/ -m J1234+5678.meta -c J1234+5678_cfg.json \
-o J1234+5678_output/
```

Here, the `-i` argument is the input directory, the `-m` option provides the meta file containing the list of archives to be processed, the `-c` argument provides the configuration file, and the `-o` argument provides the output directory.

## REFERENCES

- Agazie, G., Anumalapudi, A., Archibald, A. M., et al. 2023a, *ApJL*, 951, L8, doi: [10.3847/2041-8213/acdac6](https://doi.org/10.3847/2041-8213/acdac6)
- Agazie, G., Alam, M. F., Anumalapudi, A., et al. 2023b, *ApJL*, 951, L9, doi: [10.3847/2041-8213/acda9a](https://doi.org/10.3847/2041-8213/acda9a)
- Agazie, G., Anumalapudi, A., Archibald, A. M., et al. 2023c, *ApJL*, 951, L10, doi: [10.3847/2041-8213/acda88](https://doi.org/10.3847/2041-8213/acda88)
- Alam, M. F., Arzoumanian, Z., Baker, P. T., et al. 2021a, *The Astrophysical Journal Supplement*, 252, 5, doi: [10.3847/1538-4365/abc6a1](https://doi.org/10.3847/1538-4365/abc6a1)
- . 2021b, *The Astrophysical Journal Supplement*, 252, 4, doi: [10.3847/1538-4365/abc6a0](https://doi.org/10.3847/1538-4365/abc6a0)
- Alpar, M. A., Cheng, A. F., Ruderman, M. A., & Shaham, J. 1982, *Nature*, 300, 728, doi: [10.1038/300728a0](https://doi.org/10.1038/300728a0)
- Astropy Collaboration, Robitaille, T. P., Tollerud, E. J., et al. 2013, *A&A*, 558, A33, doi: [10.1051/0004-6361/201322068](https://doi.org/10.1051/0004-6361/201322068)
- Astropy Collaboration, Price-Whelan, A. M., Sipőcz, B. M., et al. 2018, *AJ*, 156, 123, doi: [10.3847/1538-3881/aabc4f](https://doi.org/10.3847/1538-3881/aabc4f)
- Astropy Collaboration, Price-Whelan, A. M., Lim, P. L., et al. 2022, *ApJ*, 935, 167, doi: [10.3847/1538-4357/ac7c74](https://doi.org/10.3847/1538-4357/ac7c74)
- Bhattacharya, D., & van den Heuvel, E. P. J. 1991, *PhR*, 203, 1, doi: [10.1016/0370-1573\(91\)90064-S](https://doi.org/10.1016/0370-1573(91)90064-S)
- Burgio, G. F., Schulze, H. J., Vidaña, I., & Wei, J. B. 2021, *Progress in Particle and Nuclear Physics*, 120, 103879, doi: [10.1016/j.pnpnp.2021.103879](https://doi.org/10.1016/j.pnpnp.2021.103879)
- Burnham, K. P., & Anderson, D. R. 2004, *Sociological Methods & Research*, 33, 261, doi: [10.1177/0049124104268644](https://doi.org/10.1177/0049124104268644)
- CHIME/Pulsar Collaboration, Amiri, M., Bandura, K. M., et al. 2021, *ApJS*, 255, 5, doi: [10.3847/1538-4365/abfdcb](https://doi.org/10.3847/1538-4365/abfdcb)
- Damour, T., & Deruelle, N. 1985, *Ann. Inst. Henri Poincaré Phys. Théor*, 43, 107
- . 1986, *Ann. Inst. Henri Poincaré Phys. Théor*, 44, 263
- Damour, T., & Taylor, J. H. 1991, *ApJ*, 366, 501, doi: [10.1086/169585](https://doi.org/10.1086/169585)
- . 1992, *PhRvD*, 45, 1840, doi: [10.1103/PhysRevD.45.1840](https://doi.org/10.1103/PhysRevD.45.1840)
- Deller, A. T., Vigeland, S. J., Kaplan, D. L., et al. 2016, *ApJ*, 828, 8, doi: [10.3847/0004-637X/828/1/8](https://doi.org/10.3847/0004-637X/828/1/8)
- Demorest, P. B. 2007, PhD thesis, University of California, Berkeley
- Desvignes, G., Caballero, R. N., Lentati, L., et al. 2016, *MNRAS*, 458, 3341, doi: [10.1093/mnras/stw483](https://doi.org/10.1093/mnras/stw483)
- Dickey, J. M. 1971, *The Annals of Mathematical Statistics*, 42, 204, doi: [10.1214/aoms/1177693507](https://doi.org/10.1214/aoms/1177693507)
- Ding, H., Deller, A. T., Freire, P., et al. 2020, *The Astrophysical Journal*, 896, 85, doi: [10.3847/1538-4357/ab8f27](https://doi.org/10.3847/1538-4357/ab8f27)
- Ding, H., Deller, A. T., Stappers, B. W., et al. 2023, *MNRAS*, 519, 4982, doi: [10.1093/mnras/stac3725](https://doi.org/10.1093/mnras/stac3725)

- Edwards, R. T., Hobbs, G. B., & Manchester, R. N. 2006, *MNRAS*, 372, 1549, doi: [10.1111/j.1365-2966.2006.10870.x](https://doi.org/10.1111/j.1365-2966.2006.10870.x)
- Ellis, J. A., Vallisneri, M., Taylor, S. R., & Baker, P. T. 2020, ENTERPRISE: Enhanced Numerical Toolbox Enabling a Robust Pulsar Inference Suite, v3.0.0, Zenodo, doi: [10.5281/zenodo.4059815](https://doi.org/10.5281/zenodo.4059815)
- EPTA Collaboration, InPTA Collaboration, Antoniadis, J., et al. 2023, *A&A*, 678, A50, doi: [10.1051/0004-6361/202346844](https://doi.org/10.1051/0004-6361/202346844)
- Fonseca, E., Cromartie, H. T., Pennucci, T. T., et al. 2021, *ApJL*, 915, L12, doi: [10.3847/2041-8213/ac03b8](https://doi.org/10.3847/2041-8213/ac03b8)
- Freire, P. C. C., & Wex, N. 2010, *MNRAS*, 409, 199, doi: [10.1111/j.1365-2966.2010.17319.x](https://doi.org/10.1111/j.1365-2966.2010.17319.x)
- Good, D. C. 2021, PhD thesis, University of British Columbia, doi: <http://dx.doi.org/10.14288/1.0401783>
- GRAVITY Collaboration, Abuter, R., Amorim, A., et al. 2021, *A&A*, 647, A59, doi: [10.1051/0004-6361/202040208](https://doi.org/10.1051/0004-6361/202040208)
- Hankins, T. H., & Rickett, B. J. 1986, *ApJ*, 311, 684, doi: [10.1086/164807](https://doi.org/10.1086/164807)
- Harris, C. R., Millman, K. J., van der Walt, S. J., et al. 2020, *Nature*, 585, 357, doi: [10.1038/s41586-020-2649-2](https://doi.org/10.1038/s41586-020-2649-2)
- Hazboun, J. S., Simon, J., Madison, D. R., et al. 2022, *ApJ*, 929, 39, doi: [10.3847/1538-4357/ac5829](https://doi.org/10.3847/1538-4357/ac5829)
- Hellings, R. W., & Downs, G. S. 1983, *ApJL*, 265, L39, doi: [10.1086/183954](https://doi.org/10.1086/183954)
- Holmberg, J., & Flynn, C. 2004, *MNRAS*, 352, 440, doi: [10.1111/j.1365-2966.2004.07931.x](https://doi.org/10.1111/j.1365-2966.2004.07931.x)
- Hotan, A. W., van Straten, W., & Manchester, R. N. 2004, *PASA*, 21, 302, doi: [10.1071/AS04022](https://doi.org/10.1071/AS04022)
- Hunter, J. D. 2007, *Computing in Science & Engineering*, 9, 90, doi: [10.1109/MCSE.2007.55](https://doi.org/10.1109/MCSE.2007.55)
- Johnson, A. D., Meyers, P. M., Baker, P. T., et al. 2024, *PhRvD*, 109, 103012, doi: [10.1103/PhysRevD.109.103012](https://doi.org/10.1103/PhysRevD.109.103012)
- Jones, M. L., McLaughlin, M. A., Lam, M. T., et al. 2017, *ApJ*, 841, 125, doi: [10.3847/1538-4357/aa73df](https://doi.org/10.3847/1538-4357/aa73df)
- Kirichenko, A. Y., Zharikov, S. V., Zyuzin, D. A., et al. 2018, *MNRAS*, 480, 1950, doi: [10.1093/mnras/sty1978](https://doi.org/10.1093/mnras/sty1978)
- Kopeikin, S. M. 1996, *ApJL*, 467, L93, doi: [10.1086/310201](https://doi.org/10.1086/310201)
- Lange, C., Camilo, F., Wex, N., et al. 2001, *Monthly Notices of the Royal Astronomical Society*, 326, 274, doi: [10.1046/j.1365-8711.2001.04606.x](https://doi.org/10.1046/j.1365-8711.2001.04606.x)
- Lazaridis, K., Wex, N., Jessner, A., et al. 2009, *MNRAS*, 400, 805, doi: [10.1111/j.1365-2966.2009.15481.x](https://doi.org/10.1111/j.1365-2966.2009.15481.x)
- Lee, G., Gommers, R., Waselewski, F., Wohlfahrt, K., & O’Leary, A. 2019, *The Journal of Open Source Software*, 4, 1237, doi: [10.21105/joss.01237](https://doi.org/10.21105/joss.01237)
- Lorimer, D. R. 2008, *Living Reviews in Relativity*, 11, 8, doi: [10.12942/lrr-2008-8](https://doi.org/10.12942/lrr-2008-8)
- Lorimer, D. R., & Kramer, M. 2012, *Handbook of Pulsar Astronomy* (Cambridge University Press)
- Luo, J., Ransom, S., Demorest, P., et al. 2021, *ApJ*, 911, 45, doi: [10.3847/1538-4357/abe62f](https://doi.org/10.3847/1538-4357/abe62f)
- Mata Sánchez, D., Istrate, A. G., van Kerkwijk, M. H., Breton, R. P., & Kaplan, D. L. 2020, *Monthly Notices of the Royal Astronomical Society*, 494, 4031, doi: [10.1093/mnras/staa983](https://doi.org/10.1093/mnras/staa983)
- McGaugh, S. S. 2018, *Research Notes of the American Astronomical Society*, 2, 156, doi: [10.3847/2515-5172/aadd4b](https://doi.org/10.3847/2515-5172/aadd4b)
- Miles, M. T., Shannon, R. M., Bailes, M., et al. 2023, *MNRAS*, 519, 3976, doi: [10.1093/mnras/stac3644](https://doi.org/10.1093/mnras/stac3644)
- Miles, M. T., Shannon, R. M., Reardon, D. J., et al. 2025, *MNRAS*, 536, 1489, doi: [10.1093/mnras/stae2571](https://doi.org/10.1093/mnras/stae2571)
- Moran, A., Mingarelli, C. M. F., Bedell, M., Good, D., & Spergel, D. N. 2023, *ApJ*, 954, 89, doi: [10.3847/1538-4357/acec75](https://doi.org/10.3847/1538-4357/acec75)
- Moran, A., Mingarelli, C. M. F., Van Tilburg, K., & Good, D. 2024, *PhRvD*, 109, 123015, doi: [10.1103/PhysRevD.109.123015](https://doi.org/10.1103/PhysRevD.109.123015)
- NANOGrav Collaboration, Arzoumanian, Z., Brazier, A., et al. 2015, *The Astrophysical Journal*, 813, 65, doi: [10.1088/0004-637X/813/1/65](https://doi.org/10.1088/0004-637X/813/1/65)
- Nice, D. J., & Taylor, J. H. 1995, *ApJ*, 441, 429, doi: [10.1086/175367](https://doi.org/10.1086/175367)
- Özel, F., & Freire, P. 2016, *ARA&A*, 54, 401, doi: [10.1146/annurev-astro-081915-023322](https://doi.org/10.1146/annurev-astro-081915-023322)
- Pennucci, T. T. 2019, *The Astrophysical Journal Supplement*, 871, 34, doi: [10.3847/1538-4357/aaf6ef](https://doi.org/10.3847/1538-4357/aaf6ef)
- Pennucci, T. T., Demorest, P. B., & Ransom, S. M. 2014, *ApJ*, 790, 93, doi: [10.1088/0004-637X/790/2/93](https://doi.org/10.1088/0004-637X/790/2/93)
- Perera, B. B. P., DeCesar, M. E., Demorest, P. B., et al. 2019, *MNRAS*, 490, 4666, doi: [10.1093/mnras/stz2857](https://doi.org/10.1093/mnras/stz2857)
- Phinney, E. S. 1992, *Philosophical Transactions: Physical Sciences and Engineering*, 341, 39. <http://www.jstor.org/stable/53911>
- Reardon, D. J., Shannon, R. M., Cameron, A. D., et al. 2021, *MNRAS*, 507, 2137, doi: [10.1093/mnras/stab1990](https://doi.org/10.1093/mnras/stab1990)
- Reardon, D. J., Zic, A., Shannon, R. M., et al. 2023, *ApJL*, 951, L6, doi: [10.3847/2041-8213/acdd02](https://doi.org/10.3847/2041-8213/acdd02)
- Shamohammadi, M., Bailes, M., Flynn, C., et al. 2024, *MNRAS*, 530, 287, doi: [10.1093/mnras/stae016](https://doi.org/10.1093/mnras/stae016)
- Shapiro, I. I. 1964, *PhRvL*, 13, 789, doi: [10.1103/PhysRevLett.13.789](https://doi.org/10.1103/PhysRevLett.13.789)
- Shklovskii, I. S. 1970, *Soviet Ast.*, 13, 562
- Splaver, E. M., Nice, D. J., Arzoumanian, Z., et al. 2002, *ApJ*, 581, 509, doi: [10.1086/344202](https://doi.org/10.1086/344202)
- Susobhanan, A. 2026, *abhisrckcl/chimera: chimera v0.1.0, v0.1.0*, Zenodo, doi: [10.5281/zenodo.18458818](https://doi.org/10.5281/zenodo.18458818)

- Susobhanan, A., Maan, Y., Joshi, B. C., et al. 2021, PASA, 38, e017, doi: [10.1017/pasa.2021.12](https://doi.org/10.1017/pasa.2021.12)
- Susobhanan, A., Kaplan, D. L., Archibald, A. M., et al. 2024, ApJ, 971, 150, doi: [10.3847/1538-4357/ad59f7](https://doi.org/10.3847/1538-4357/ad59f7)
- Taylor, J. H., & Weisberg, J. M. 1982, ApJ, 253, 908, doi: [10.1086/159690](https://doi.org/10.1086/159690)
- The CHIME Collaboration, Amiri, M., Bandura, K., et al. 2022, arXiv e-prints, arXiv:2201.07869. <https://arxiv.org/abs/2201.07869>
- Tiburzi, C., Verbiest, J. P. W., Shaifullah, G. M., et al. 2019, MNRAS, 487, 394, doi: [10.1093/mnras/stz1278](https://doi.org/10.1093/mnras/stz1278)
- van Straten, W. 2026, PASP, 138, 013001, doi: [10.1088/1538-3873/ae20bf](https://doi.org/10.1088/1538-3873/ae20bf)
- van Straten, W., & Bailes, M. 2011, PASA, 28, 1, doi: [10.1071/AS10021](https://doi.org/10.1071/AS10021)
- Wahl, H. M., McLaughlin, M. A., Gentile, P. A., et al. 2022, ApJ, 926, 168, doi: [10.3847/1538-4357/ac4045](https://doi.org/10.3847/1538-4357/ac4045)
- Xu, H., Chen, S., Guo, Y., et al. 2023, Research in Astronomy and Astrophysics, 23, 075024, doi: [10.1088/1674-4527/acdfa5](https://doi.org/10.1088/1674-4527/acdfa5)
- You, X. P., Coles, W. A., Hobbs, G. B., & Manchester, R. N. 2012, MNRAS, 422, 1160, doi: [10.1111/j.1365-2966.2012.20688.x](https://doi.org/10.1111/j.1365-2966.2012.20688.x)